JGR Atmospheres

RESEARCH ARTICLE
10.1029/2025JD045172

Observation of Mountain Waves and Secondary Gravity Waves in the Mesosphere Lower Thermosphere Above Patagonia

Robert Reichert[1,2], Pierre-Dominique Pautet[3], Bernd Kaifler[1], Sebastian Rhode[4], Jörn Ungermann[4], Kaoru Sato[5], Diego Janches[6], and Steven Smith[7]

[1]Deutsches Zentrum für Luft- und Raumfahrt, Institut für Physik der Atmosphäre, Wessling, Germany, [2]Meteorological Institute Munich, Ludwig-Maximilians-Universität, Munich, Germany, [3]Center for Atmospheric and Space Sciences/Physics Department, State University, Logan, UT, USA, [4]Institute of Energy and Climate Research, Stratosphere (IEK-7), Forschungszentrum Jülich, Jülich, Germany, [5]Department of Earth and Planetary Science, The University of Tokyo, Tokyo, Japan, [6]NASA GSFC, Washington, DC, USA, [7]Center for Space Physics, Boston University, Boston, MA, USA

Key Points:

- We observed mountain and secondary gravity waves in the OH layer above Tierra del Fuego using co-located ground-based instruments
- Mountain wave breaking near 63 km likely generated fast secondary waves later seen above Tierra del Fuego after a turning level vanished
- A novel retrieval method quantifies momentum flux from wave features and includes uncertainties from measurements and OH layer variability

Supporting Information:

Supporting Information may be found in the online version of this article.

Correspondence to:

R. Reichert,
robert.reichert@physik.uni-muenchen.de

Citation:

Reichert, R., Pautet, P.-D., Kaifler, B., Rhode, S., Ungermann, J., Sato, K., et al. (2026). Observation of mountain waves and secondary gravity waves in the mesosphere lower thermosphere above Patagonia. *Journal of Geophysical Research: Atmospheres*, *131*, e2025JD045172. https://doi.org/10.1029/2025JD045172

Received 27 AUG 2025
Accepted 22 FEB 2026

Abstract We find observational evidence for mountain waves (MWs) and secondary gravity waves (2GWs) in the OH*(3-1) layer above Tierra del Fuego, Argentina. On the night of 21–22 May 2018, the Advanced Mesospheric Temperature Mapper (AMTM) obtained temperatures at ∼84 km. During the westerly phase of the semi-diurnal tide, arc-shaped quasi-stationary structures in temperature maps indicated MWs with horizontal wavelengths of 20–40 km. A co-located temperature measurement from the COmpact Rayleigh Autonomous Lidar (CORAL) confirmed quasi-stationary structures down to 15 km, also indicating MWs. Temperature profiles revealed a convectively unstable region within a MW phase front at 58–66 km—a sign of MW breaking, momentum deposition, local body forces, and generation of 2GWs. After a wind reversal in the mesosphere/lower thermosphere (MLT) observed by the Southern Argentina Agile Meteor Radar (SAAMER), a gravity wave propagated southeastward with an intrinsic phase speed >90 ms^{-1}. Using 1-D cross-wavelet analysis, we derived spectral properties of this fast wave and performed ray-tracing, using the Japanese Whole Atmosphere Reanalysis as background. The fast wave likely originated near 63 km above the Torres del Paine region, known for large-amplitude MWs. We conclude that tropospheric forcing excites MWs over Tierra del Fuego (observed) and over the Torres del Paine massif (not observed) ∼500 km northwest. The latter MWs likely generate 2GWs upon breaking in the lower mesosphere, observed over Tierra del Fuego after a turning-level disappearance. A novel momentum-flux (MF) retrieval, based on co-located AMTM, CORAL, and SAAMER measurements, automatically identifies dominant wave features, incorporating measurement and OH*(3-1) layer variability to infer realistic MF uncertainties.

Plain Language Summary On the night of 21–22 May 2018, atmospheric scientists observed mountain waves and secondary gravity waves above Tierra del Fuego, Argentina. Clear skies allowed continuous temperature measurements near 84 km altitude using a camera. The data showed patterns typical of mountain waves, triggered when strong winds blow over mountains. Additional temperature data from a co-located laser system confirmed these waves extended downward to about 15 km. In one region between 58 and 66 km, the atmosphere was unstable—a sign that mountain waves were breaking and transferring energy into ambient wind. This process can generate new waves, known as secondary gravity waves. Later in the night, after a shift in wind direction, a fast-moving wave was detected traveling southeast at over 90 ms^{-1}. Analysis suggested this wave originated around 63 km altitude above the Torres del Paine mountains, about 500 km northwest. Breaking of mountain waves may have created the fast-moving wave, classifying it as secondary. These conclusions were enabled by a new analysis method that automatically identifies and measures wave properties using co-located temperature and wind observations. The method also accounts for measurement uncertainties, enabling an accurate estimate of how much momentum these waves carry into the upper atmosphere.

1. Introduction

Atmospheric gravity waves (GWs) are traveling perturbations in the stably stratified atmosphere. As they travel along three-dimensional trajectories, they transport energy and horizontal pseudo-momentum vertically from their source regions to the locations where they dissipate. This vertical transport of horizontal momentum,

referred to as GW momentum flux (MF), influences atmospheric circulation and structure at higher altitudes (Fritts & Alexander, 2003). This process is particularly important in the mesosphere and lower thermosphere (MLT), where, due to energy conservation and decreasing density, GW amplitudes grow until nonlinear processes —such as overturning and breaking—occur. These processes lead to localized momentum deposition that accelerates the background flow. It is hypothesized that such body forces can in turn generate new waves, which propagate upward and carry a fraction of the deposited momentum into even higher altitudes. These are termed secondary gravity waves (2GWs) (e.g., Bossert et al., 2017; Vadas et al., 2018). The process of wave dissipation and generation of higher-order GWs that transport momentum to higher altitudes is referred to as multistep vertical coupling (Becker & Vadas, 2020; Vadas & Becker, 2019).

Harvey et al. (2022) compared zonal-mean zonal winds from the Sounding of the Atmosphere using Broadband Emission Radiometry (SABER) observations with those from the WACCMX + DART model during southern hemisphere winter and found a $\sim 30\,\mathrm{ms}^{-1}$ discrepancy above ~ 80 km altitude poleward of 40°S, with the model erroneously predicting easterlies. They concluded that a contributing factor is the omission of higher-order waves such as 2GWs in the model. To understand and eventually reduce such biases, observational evidence for multistep vertical coupling is required.

GW signatures in the MLT were first identified in meteor radar (MR) wind observations as early as the 1950s (Greenhow & Neufeld, 1959; Manning et al., 1950), and Hines (1960) later confirmed their origin. By the 1970s, GW-induced fluctuations were also observed in the OH*(3-1) airglow layer near ~ 87 km altitude (Krassovsky et al., 1975; Moreels & Herse, 1977; Noxon, 1978; Peterson & Kieffaber, 1973). Advances in instrumentation have since led to high-resolution airglow imagers capable of resolving features down to 17 m spatially and 2.5 s temporally (Sedlak et al., 2016), enabling the study of small-scale GWs and turbulence. While airglow intensity measurements are valuable for estimating GW horizontal scales, propagation directions, phase speeds, localization, intermittency, and sources, they are less reliable for MF estimation due to their sensitivity to temperature, pressure, and chemical composition. A major advancement came with the Advanced Mesospheric Temperature Mapper (AMTM), which measures OH*(3-1) band intensity at three wavelengths to derive rotational temperatures (Pautet et al., 2014). When combined with co-located measurements of background wind and stratification, such data enable the estimation of MF with an accuracy of $\sim 40\%$ (Fritts et al., 2014). Fritts et al. (2014) demonstrated this capability by manually analyzing visually prominent wave events from two nights of AMTM–lidar–MR data. They called for the development of automated approaches to identify and characterize GWs more routinely, allowing for robust statistical studies. Responding to that call, Pautet et al. (2021) analyzed 97 nights of AMTM data to quantify mountain wave (MW)-driven momentum fluxes. However, they assumed a fixed Brunt–Väisälä frequency ($N = 0.02\,\mathrm{s}^{-1}$) and a constant OH*(3-1) layer peak altitude and thickness, which proved to be too restrictive: in 61 of 97 cases, vertical wavelengths derived from the dispersion relation were either indeterminate or too small ($\ll 10$ km) for the AMTM to be capable to detect them. Reichert et al. (2019) addressed this limitation by combining airglow, lidar, and MR data with a 1-D wavelet decomposition and a phase-line tracking algorithm to estimate intrinsic GW parameters. In this study, we build upon that approach and, inspired by Wright et al. (2021), apply a 2-D continuous wavelet transform (CWT) to analyze phase differences between consecutive temperature maps. This allows us to extract observed frequencies and phase speeds with improved spatial coverage and temporal resolution.

Despite growing theoretical and modeling interest, direct observations of 2GWs remain rare. During the DEEPWAVE campaign in New Zealand in 2014, Bossert et al. (2015, 2017) detected GWs with horizontal wavelengths in the range of $\lambda_h \approx 10-30$ km above large-scale MWs ($\lambda_h \approx 200-240$ km) using airborne Rayleigh lidar measurements. They interpreted the small-scale waves as 2GWs, supported by AMTM and MR data, and estimated their MF at more than $100\,\mathrm{m}^2\,\mathrm{s}^{-2}$. Kogure et al. (2020) linked Atmospheric InfraRed Sounder (AIRS) observations of large-scale MWs ($\lambda_h \approx 500$ km) over the southern Andes at ~ 40 km altitude with concentric ring-like structures in Visible/Infrared Imaging Radiometer Suite (VIIRS) OH airglow imagery (~ 87 km), characterized by shorter wavelengths ($\lambda_h \approx 100$ km). Notably, both studies observed 2GWs with horizontal scales smaller than those of their respective primary MWs. However, theoretical work by Vadas et al. (2018) suggests the opposite scaling: that 2GWs should have horizontal wavelengths roughly 8 times that of the primary wave. This scaling has been supported by lidar observations at McMurdo and ALOMAR, which revealed repeating "fishbone" patterns associated with multistep coupling (Vadas et al., 2023). Using SABER data, Liu et al. (2019) provided global climatologies of both primary and secondary GW activity, while Vadas and

Azeem (2021) documented 2GWs in the ionosphere as concentric GPS-TEC perturbations driven by tropospheric convection.

In this study, we present a new observation of 2GWs based on ground-based measurements at the Estación Astronómica Río Grande (EARG) (53.7°S, 67.7°W) in the lee of the southern Andes—using the same suite of instruments as during the DEEPWAVE campaign, but in a different geographic and dynamic setting. In contrast to Bossert et al. (2015, 2017), we observe small-scale MWs ($\lambda_h \approx 20-40$ km) followed a few hours later by large-scale ($\lambda_h \approx 170$ km) waves propagating with a phase speed of $|\hat{\boldsymbol{c}}| \approx 90\,\mathrm{ms}^{-1}$ in the OH*(3-1) layer. Building on previous studies (Fritts et al., 2014; Pautet et al., 2021; Reichert et al., 2019), we refine the spectral analysis and develop a two-stage Monte Carlo–based (MC^2) MF retrieval to enable routine, objective analysis without reliance on manually selected wave packets. The ultimate goal is to apply this method to a full year of co-located observations to derive statistically robust GW climatologies in the MLT over Tierra del Fuego.

In the present study, we focus on the following hypothesis:

1. The application of wavelet analysis and Monte Carlo simulations to co-located airglow-lidar-MR measurements enables the retrieval of GWMFs and associated uncertainties in an automatic fashion.
2. 2GWs are generated in the lower mesosphere over Torres del Paine upon the breaking of MWs, propagate southeastward over Patagonia, and are observed over Tierra del Fuego.

The manuscript is structured as follows: Section 2 describes the AMTM, CORAL, SAAMER, and JAWARA data sets. Section 3 outlines the methodology, including the MC^2-MF retrieval (with further details in the Appendix). Section 4 presents time-varying distributions of key GW properties such as amplitudes, wavelengths, phase speeds, and MFs for GWs smaller and larger than the FOV of the AMTM. Section 5 places the observations in a broader dynamical context using analyses from the Integrated Forecast System of the European Centre for Medium-Range Weather Forecasts and a linear-theory-based ray tracer to aid interpretation. Finally, Section 6 summarizes the study and provides concluding remarks.

2. Data Sets

2.1. Temperature Observations With the AMTM

The AMTM is an instrument developed at Utah State University to measure nighttime atmospheric temperatures over a 200 × 160 km area centered at the zenith. It uses the OH*(3-1) band emission, originating from a layer at ∼87 km in altitude, to trace mesospheric dynamics (Pautet et al., 2014). Equipped with a 320 × 256-pixel infrared sensor, the AMTM captures sequential brightness measurements of specific OH*(3-1) band lines to calculate rotational temperatures (here after referred to as temperatures) across each pixel, creating high-resolution temperature maps every ∼35 s with ∼0.625 km/pixel spatial accuracy at the zenith and ∼1 K precision. Such high-resolution temperature maps allow for the analysis of GW characteristics, dissipation, instabilities, and MF. GWs propagating through the field of view (FOV) of the imager manifest themselves as temperature fluctuations with spatial scales ranging from ∼10 km (Hecht et al., 2018; Pautet et al., 2021) to even 4,000 km (Fritts et al., 2014). Latter GWs are too large to be identified as a wave pattern in one single temperature map. However, if the observed period is small enough, comparing spatially separated time series, it is possible to derive a horizontal wavelength that is larger than the AMTM's FOV via the phase shift between two time series.

In this work, we are studying AMTM data from Río Grande, Argentina, obtained on the night of 21–22 May 2018. This night was mostly clear with only few clouds just before dawn. Figure 1 contextualizes the two key measurements of OH*(3-1) band intensity that form the basis of this study by placing them in a geographic setting. At 04:00 UTC, arc-shaped, quasi-stationary structures with short horizontal wavelengths ($\lambda_h \approx 20-40$ km) are observed above the measurement site, located in the relatively flat eastern region of Tierra del Fuego. The mountain peaks beneath the intensity map remain below 1,000 m in elevation. The highest peak in the vicinity is Mount Darwin (2,568 m), located approximately 150 km southwest of Río Grande. At the 700 hPa level (∼3 km), the flow is westerly, with horizontal wind speeds of $|\boldsymbol{u}| = 10-15\,\mathrm{ms}^{-1}$ according to ERA5 reanalysis data (Hersbach et al., 2020). By 08:00 UTC, the previously observed quasi-stationary structures have disappeared, and a larger-scale ($\lambda_h \approx 170$ km) wave structure enters the scene, propagating from northwest to southeast. Meanwhile, the lower-level wind conditions remain largely unchanged. To provide additional context, Figure 2 presents the AMTM observation in a keogram format (Taylor et al., 2009). The keogram condenses the three-

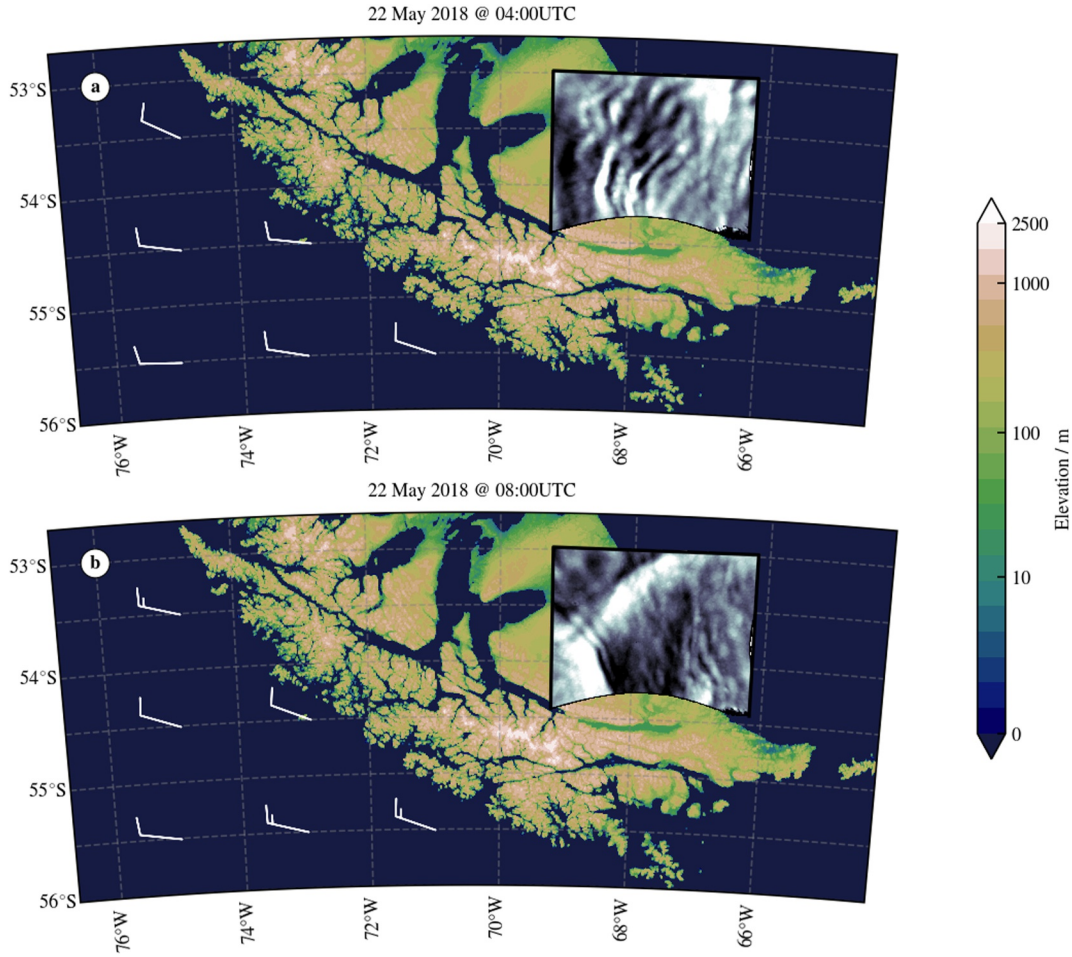

Figure 1. Topography of the southern Andes and AMTM OH*(3-1) band intensity (greyscale image) on 22 May 2018 at (a) 04:00 UTC and (b) 08:00 UTC. White wind barbs indicate the 700 hPa wind field upstream of the Andes, taken from ERA5 reanalysis.

dimensional data set by stacking rows (for east-west views) and columns (for north-south views) of pixels. Since complementary lidar measurements are available, we construct keograms aligned with the rows and columns corresponding to the lidar beam position. To analyze the coexistence of small- and large-scale structures, we decompose the AMTM temperature field into four components:

$$T(x,y,t) = T_{\mathrm{bg}}(t) + T_{\mathrm{large}}(x,y,t) + T_{\mathrm{small}}(x,y,t) + T_{\mathrm{noise}}(x,y,t) \quad (1)$$

The background temperature $T_{\mathrm{bg}}(t)$ consists of a nightly FOV-mean, augmented by tidal oscillations with periods of 24, 12, and 8 hr. For the night analyzed, we find a mean temperature of 203.2 K, with tidal amplitudes of 1.3 K (diurnal), 10.8 K (semi-diurnal), and 8.3 K (ter-diurnal), respectively. Subsequently, we identify linear trends and the first harmonics from a 2-D fast Fourier transform (FFT) for each map of residual temperatures. This allows us to separate large-scale (>100 km) temperature perturbations T_{large} from small-scale (<100 km) ones T_{small}. To reduce noise, we apply Gaussian smoothing to T_{small} with standard deviations $\sigma = [1.25\,\mathrm{km}, 1.25\,\mathrm{km}, 70\,\mathrm{s}]$ in the respective dimensions. Figures 2a and 2b show the full temperature field T, where tidal oscillations are still visible. Figures 2c and 2d depict T_{large}, revealing thermal structures that exceed the FOV in scale. The large-scale feature seen in Figure 1b is a snapshot from two positive and two negative phase lines migrating west-to-east (panel c) and north-to-south (panel d) between 07:30 UTC and 08:30 UTC. The observed phase migration, when combined with the wave period, permits estimation of the horizontal wavelength of GWs even when their full structure lies beyond the FOV (see e.g. Fritts et al., 2014; Reichert et al., 2019). A particularly prominent

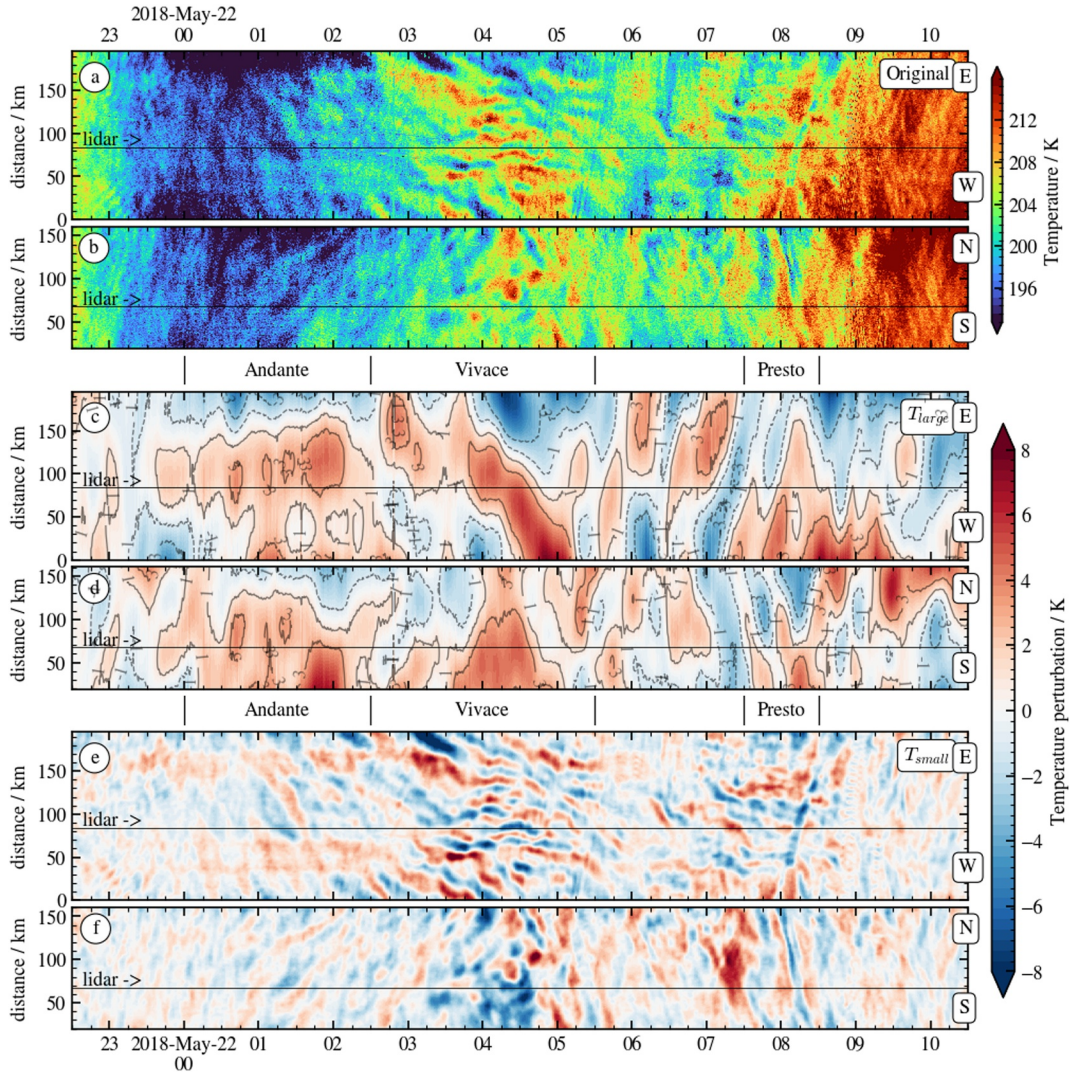

Figure 2. AMTM temperature measurement on 21–22 May 2018 as keogram representation. Temperature keogram in zonal (a) and meridional (b) direction with a resolution of 35 s and 625 m. Large-scale temperature structures T_{large} as zonal (c) and meridional (d) keograms. Small-scale temperature fluctuations T_{small} as zonal (e) and meridional (f) keograms. Thin black lines mark the position of CORAL's laser beam.

positive phase line is seen migrating east-to-west in panel c between 03:30 UTC and 05:00 UTC. Figures 2e and 2f present T_{small}, illustrating sub-FOV-scale thermal structures. Notable are quasi-stationary patterns in the zonal direction (panel e) during 02:30–05:30 UTC, coinciding with the measurements shown in Figure 1a. For reference throughout this study, we divide the AMTM observation period into three distinct intervals: *Andante* (00:00–02:30 UTC), representing a relatively calm stage; *Vivace* (02:30–05:30 UTC), characterized by enhanced quasi-stationary wave activity; and *Presto* (07:30–08:30 UTC) during which fast-propagating GWs dominate.

2.2. Temperature Observations With CORAL

CORAL is an autonomous Rayleigh lidar system designed to measure nighttime temperatures in the middle atmosphere with high vertical resolution (B. Kaifler & Kaifler, 2021). Since November 2017, it has been operating at the EARG, where it is well positioned to detect GWs in the lee of the southern Andes (N. Kaifler et al., 2020; Reichert et al., 2021). The lidar data are processed to yield temperature profiles with a vertical resolution of 1.5 km and temporal resolutions of 15, 30, 60, and 120 min, as well as nightly means. Figure 3 presents CORAL observations from the night of 21–22 May 2018, covering altitudes from 15 to 95 km. Data

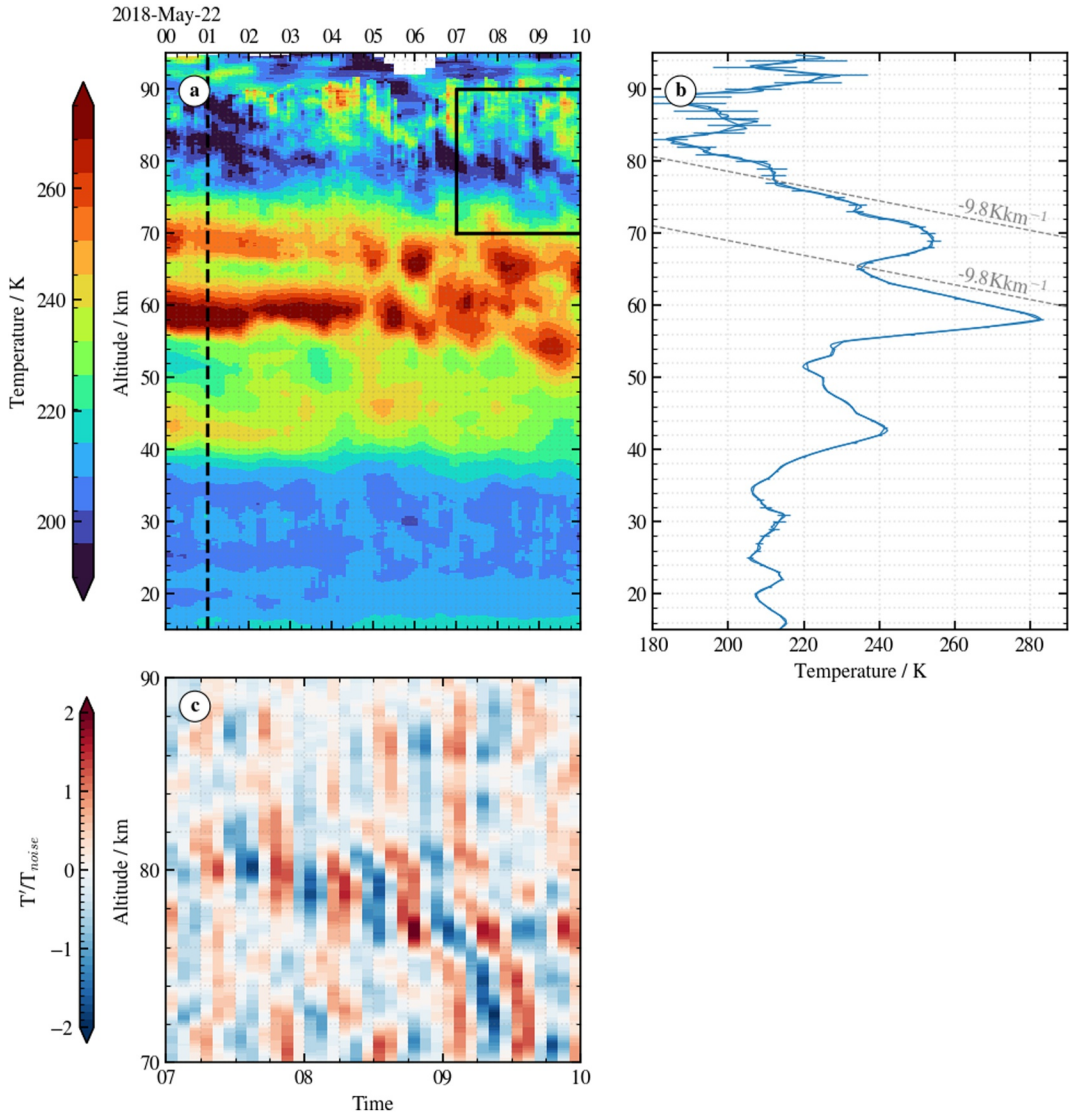

Figure 3. (a) CORAL temperature observation on the night of 21–22 May 2018. (b) CORAL temperature profile taken at 01:00 UTC. Dashed lines mark the dry adiabatic lapse rate. (c) High-pass filtered (cutoff: 0.7 hr) temperature perturbations divided by temperature uncertainty at the time of *Presto* (black box in panel a).

up to 90 km are available at 15-min resolution, while data above 90 km are resolved at 60-min intervals. Between 00:00 UTC and approximately 06:00 UTC, we observe quasi-stationary temperature structures spanning 15–70 km in altitude. The temperature profile at 01:00 UTC (Figure 3b) reveals convectively unstable layers between 58–66 km and 72–82 km, where the lapse rate approaches the dry adiabatic value. After 06:00 UTC, the thermal structures in the upper stratosphere and lower mesosphere become less coherent, and above 70 km the temperature field is increasingly dominated by small-scale fluctuations (see black box in Figure 3a). Figure 3c focuses on a high-pass-filtered (cutoff: 0.7 hr) version of the lidar data during the *Presto* interval. At altitudes corresponding to the OH*(3-1) emission layer, temperature perturbations with frequencies comparable to those observed by the AMTM are also evident. To prevent misinterpretation we divide temperature fluctuations by temperature uncertainties which are in the range of 5–15 K between 80 and 95 km resulting in a decrease of fluctuation amplitudes above ∼82 km.

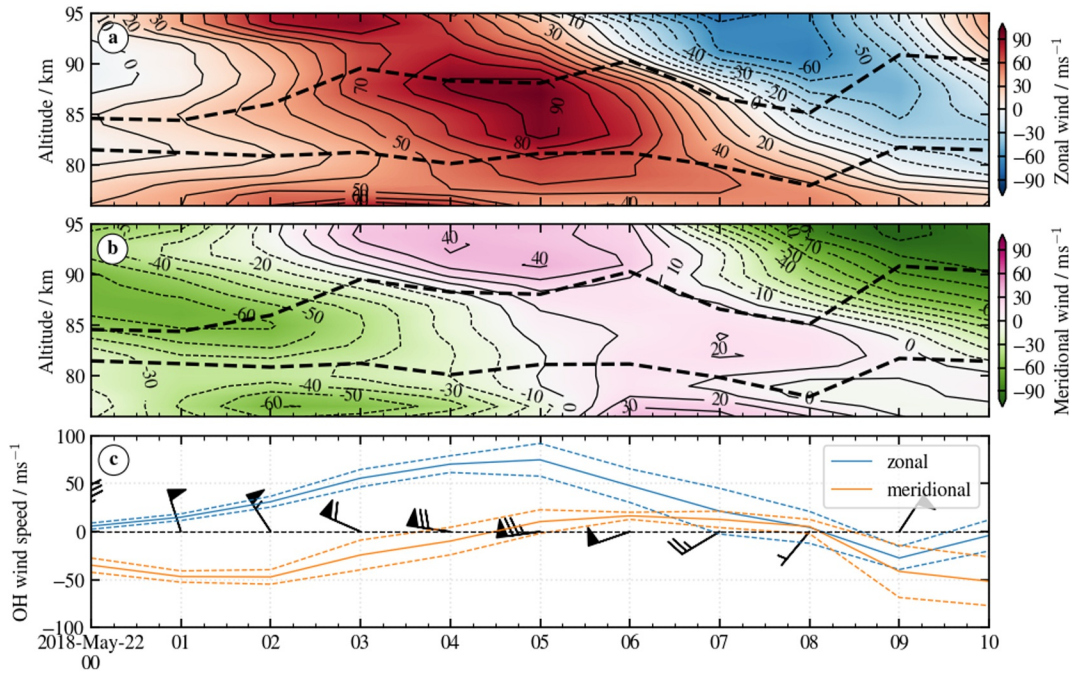

Figure 4. SAAMER zonal (a) and meridional (b) winds as function of local time and altitude. Dashed lines mark the location of the OH*(3-1) layer. Zonal (blue) and meridional (orange) winds height-averaged over the OH*(3-1) layer are illustrated in (c). Wind barbs visualize the absolute wind speed and wind direction. Dashed lines mark one standard deviation of variability over the OH*(3-1) layer.

2.3. Wind Observations With SAAMER

The SAAMER radar is specifically designed for high-resolution measurements of wind fields and the detection of GWMF through a specialized multi-beam configuration. To capture vertical motions relevant to GWs, it operates with high meteor count rates and at off-zenith angles ranging from 15° to 50°. SAAMER's significantly higher peak power compared to standard MRs allows for optimized detection in the MLT region. This configuration enables precise characterization of winds in the MLT, with recent system upgrades further enhancing the quality of data for GW studies. For a detailed technical description, the reader is referred to Fritts et al. (2010). Using the Gaussian-weighting method described by Hindley et al. (2022), SAAMER wind measurements are processed with a vertical resolution of 1 km and a temporal resolution of 1 hr. Figures 4a and 4b display the horizontal wind components as a function of time and altitude for the night of 21–22 May 2018, including the estimated location of the OH*(3-1) emission layer (see Section 3.1). A prominent feature in both zonal and meridional wind fields is the downward phase progression of alternating positive and negative wind perturbations due to tides. We apply a harmonic decomposition of the SAAMER winds taking into account a 24 hr window centered on 22 May 2018 05:00 UTC and compute the OH*(3-1) layer averaged amplitudes. We find a mean zonal and meridional wind of 29 ms^{-1} and −16 ms^{-1} respectively as well as diurnal tides of 5 ms^{-1} (zonal) and 6 ms^{-1} (meridional) amplitude, semi-diurnal tides of 44 ms^{-1} (zonal) and 35 ms^{-1} (meridional) amplitude, and ter-diurnal tides of 16 ms^{-1} (zonal) and 8 ms^{-1} (meridional) amplitude. These values are in agreement with the previous study of Stober et al. (2021).

Figure 4c shows the time series of horizontal wind components averaged over the vertical extent of the OH*(3-1) layer. During the *Andante* interval, winds are predominantly northerly at speeds of 20 − 30 ms^{-1}. These intensify and rotate to strong westerlies reaching up to 75 ms^{-1} during *Vivace*, persisting for approximately 2–3 hr. At the onset of *Presto*, a wind reversal is observed, with winds shifting to (north)easterly directions and remaining so for the remainder of the observation period.

2.4. JAWARA Reanalysis

In this study, we use wind and temperature fields from the Japanese Atmospheric General circulation model for Upper Atmosphere Research Data Assimilation System (JAGUAR-DAS) Whole Atmosphere Reanalysis

(JAWARA (Koshin et al., 2025; Sato & Koshin, 2025);) as the atmospheric background for GW raytracing. JAWARA integrates global observations of temperature from the Microwave Limb Sounder aboard the Aura satellite, SABER aboard the Thermosphere Ionosphere Mesosphere Energetics and Dynamics satellite, and radiance from the Special Sensor Microwave Imager/Sounder aboard the Defense Meteorological Satellite Program satellites into a general circulation model framework that explicitly permits GW propagation. The model simulates the dynamics of the neutral atmosphere only and extends up to 150 km altitude. With a horizontal resolution of approximately 300 km and vertical resolution of ∼1 km, JAWARA does not resolve individual GWs, but it captures the large-scale background conditions relevant for their propagation. Importantly, its zonal wind fields in the MLT have been validated against independent MR and mesosphere–stratosphere–troposphere radar observations that are not assimilated into the system (Koshin, Kohma, & Sato, 2022; Koshin, Sato, et al., 2022; Sato et al., 2023). Figure 5 juxtaposes JAWARA and SAAMER wind profiles. Generally, we find an increasing discrepancy with altitude. At 00:00 UTC the SAAMER measurement and the JAWARA reanalysis differ by up to 70 ms^{-1}. After that, it seems that the JAWARA reanalysis zonal wind is ∼3 h ahead of the SAAMER measurements. This is reflected in the early slow downward migration of the JAWARA zero-zonal wind line from ∼100 km at 01:00 UTC to 85 km at 07:00 UTC while in SAAMER it migrates faster down from >100 km at 04:00 UTC to 85 km at 07:00 UTC. It should be noted that SAAMER wind measurements are unfiltered and thus likely include GW contributions. Moreover, localized and intermittent wave–mean flow interactions within SAAMER's observational volume may contribute to non-negligible deviations from the smoother JAWARA background fields. After 07:00 UTC, JAWARA and SAAMER zonal winds exhibit better agreement. In contrast, the meridional wind profiles show no similar systematic bias; differences remain relatively minor and unsystematic. Despite some increasing divergence with altitude, the JAWARA background wind fields provide a physically consistent and observationally constrained environment. This is particularly important during the *Presto* period, when the agreement between SAAMER and JAWARA winds supports the reliability of subsequent raytracing analyses.

3. Methods

3.1. Estimation of the OH*(3-1) Emission Layer Peak Altitude and Thickness

The AMTM provides temperature measurements representing a weighted average over the OH*(3-1) layer temperature distribution (e.g., Dunker, 2018; Fritts et al., 2014; Pautet et al., 2014). To accurately analyze GW properties, we later compute height-weighted averages of atmospheric variables such as static stability and horizontal wind. This requires knowledge about the OH*(3-1) emission layer peak altitude and full width at half maximum (FWHM, here after referred to as thickness). Dunker (2018) compared nightly mean temperatures from a ground-based spectrometer and a Na lidar and states that "The OH*(3-1) layer emission altitude cannot be determined unambiguously from temperature comparison with lidars." However, when comparing temperatures regularly, that is in this study every 15 min, we gain new information on the temporal behavior of the OH*(3-1) layer properties. This additional information can be used to apply filter in the time domain and maximize correlation, minimize RMSE, and minimize temperature bias. Overall, we argue that temporal consistency can reduce the degree of ambiguity and not only the OH*(3-1) layer peak altitude but also the thickness can be derived as function of time. For details on the methodology, including data processing, filtering, bias correction procedures, and uncertainty calculations we refer to Appendix A. Overall, we find the OH*(3-1) emission layer at a peak altitude of 84.4 ± 2.7 km and with a thickness of 7.0 ± 2.4 km which is in agreement with the OH*(3-1) layer climatology (Baker & Stair, 1988). In addition, we find that OH-weighted lidar temperatures are constantly exceeding AMTM temperatures by 4.7 K which is likely due to a non-Gaussian OH-concentration profile or the temperature seeding in the top-down hydrostatic integration within the lidar temperature retrieval (Hauchecorne & Chanin, 1980; B. Kaifler & Kaifler, 2021).

3.2. Monte Carlo Based Momentum Flux Retrieval

As GWs propagate vertically through the atmosphere, they transport horizontal pseudo-momentum (Fritts & Alexander, 2003). We neglect low-frequency GWs (the part of the GW spectrum that is difficult to analyze based on our nighttime only observations) and follow Fritts et al. (2014) and Pautet et al. (2021) to compute the GWMF per unit mass according to

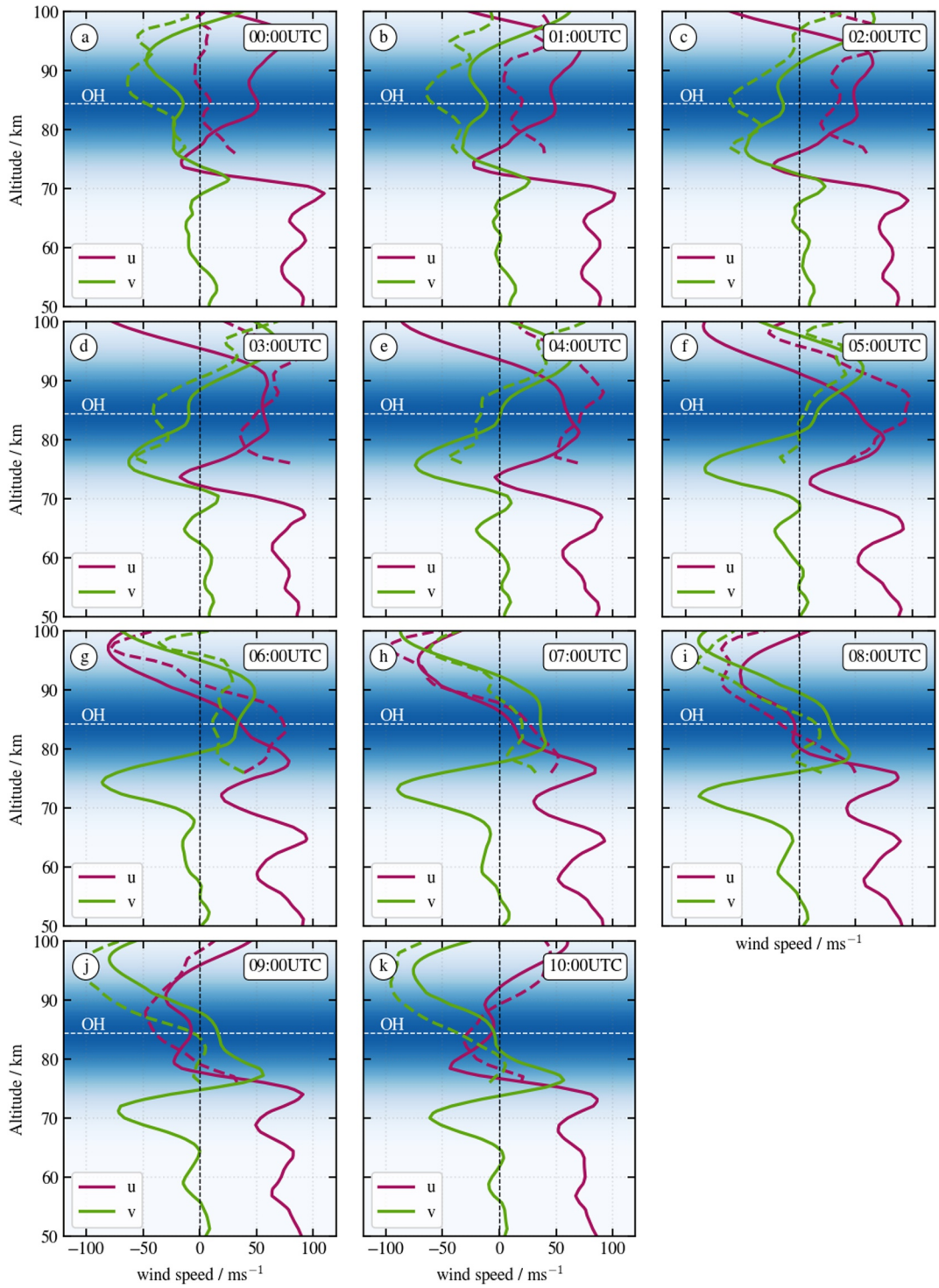

Figure 5. Zonal (red) and meridional (green) wind profiles taken from JAWARA reanalysis (solid) and from SAAMER measurements (dashed) at the location of Río Grande. Blue shading marks the nightly mean OH*(3-1) layer position. Panels (a–k) illustrate wind profiles from 00 UTC to 10 UTC.

$$\boldsymbol{F} = \frac{g^2\hat{\omega}}{2N^3}\sqrt{1-\frac{\hat{\omega}^2}{N^2}}\left(\frac{\hat{T}}{T_0}\right)^2\begin{pmatrix}\sin(\hat{\theta})\\ \cos(\hat{\theta})\end{pmatrix} \tag{2}$$

where $g = 9.54\,\mathrm{ms}^{-1}$ is the acceleration due to gravity at the OH*(3-1) layer altitude, $\hat{\theta}$ is the intrinsic propagation direction, $T_0 = T_{\mathrm{bg}} + T_{\mathrm{large}}$ is the background temperature that is perceived by smaller-scale GWs exhibiting the true temperature amplitude $\hat{T}$. The intrinsic frequency $\hat{\omega}$ is derived from the observed frequency ω taking into account the Doppler shift induced by the background wind $\boldsymbol{u}$ in direction of wave propagation, that is $\hat{\omega} = \omega - \boldsymbol{u}\cdot\boldsymbol{k}$, where $\boldsymbol{k}$ is the horizontal wave vector. Due to phase averaging over the finite thickness of the OH*(3-1) layer the measured GW temperature amplitude $\langle\hat{T}\rangle$ differs from the true GW amplitude $\hat{T}$ by a factor of C such that $\langle\hat{T}\rangle = C\hat{T}$ (see Fritts et al., 2014) where

$$C = \exp\left(-3.56\,\frac{Z_{\mathrm{FWHM}}^2}{\lambda_z^2}\right). \tag{3}$$

The AMTM temperature maps provide information on ω, $\boldsymbol{k}$, $\langle\hat{T}\rangle$, T_0, as well as observed phase speed $\boldsymbol{c}$ and observed propagation direction θ. CORAL temperature profiles enable the determination of N. The vertical wavelength of GWs with periods smaller than 30 min cannot be measured using the lidar temperature data. Therefore, we make use of the dispersion relation in order to estimate the vertical wavenumber. The dispersion relation assuming that $\hat{\omega} \gg f$ (the Coriolis frequency) is given by Nappo (2013) and reads

$$m^2 = \frac{N^2}{\hat{\boldsymbol{c}}^2} - \frac{1}{4H_s^2} - \boldsymbol{k}^2 - \frac{1}{H_{\mathrm{s}}}\frac{u_{\parallel}'}{|\hat{\boldsymbol{c}}|} + \frac{u_{\parallel}''}{|\hat{\boldsymbol{c}}|}, \tag{4}$$

where $\hat{\boldsymbol{c}}$ is the intrinsic phase speed, $H_{\mathrm{s}} = RT_0/g$ is the scale height with gas constant $R = 287.05\,\mathrm{Jkg}^{-1}\mathrm{K}^{-1}$, and $u_{\parallel}'$ and $u_{\parallel}''$ are vertical wind shear and curvature in direction of wave propagation. Equation 4 describes the full dispersion relation as we need it later for our discussion. However, in the computation of the vertical wavenumber we neglect shear and curvature terms. Please note that $T_0, \hat{T}, \hat{\omega}, \boldsymbol{k}, m, H_{\mathrm{s}}$ are considered functions of location and time, that is (x, y, t), while N, $\boldsymbol{u}$, Z_{peak}, and Z_{FWHM} are considered functions of time only. Please note further that N is measured only by CORAL at the location of the lidar beam (marked in Figure 2) and $\boldsymbol{u}$ represents a spatial average over a circle with ~300 km diameter. Uncertainties in N and $\boldsymbol{u}$ become even larger due to the imprecise knowledge of the OH*(3-1) layer altitude and thickness. The standard Gaussian error propagation cannot be applied because it is only valid for small errors and differentiable functions far away from definition limits which are in our case $\hat{\omega} \to N$ and $m^2 \to 0$. Hence, we utilize a two-stage Monte Carlo simulation, MC^2: we first generate 100 random pairs of Z_{peak} and Z_{FWHM} drawn from Gaussian distributions with standard deviations σ_{peak} and σ_{FWHM} (see their derivation in Appendix A). For each pair of Z_{peak} and Z_{FWHM} we generate 100 perturbed profiles of N and $\boldsymbol{u}$ using Gaussian noise based on measurement uncertainties σ_N and $\boldsymbol{\sigma_u}$. We then compute Gaussian-weighted averages of these perturbed profiles, yielding 10,000 realizations of N and $\boldsymbol{u}$ that incorporate uncertainty in both the OH*(3-1) layer parameters and the lidar/MR measurement uncertainties. Given additional information on $\boldsymbol{k}$ and ω from wavelet analysis applied to the AMTM temperature maps our MC^2-MF retrieval creates appropriate distributions of $\hat{\boldsymbol{c}}$, $\hat{\omega}$, m^2, and $\boldsymbol{F}$. This allows for more sophisticated analysis and interpretation of results. To identify propagating waves in the distributions, we define a wave filter that fulfills (a) $|\hat{\boldsymbol{c}}| < c_{\mathrm{s}}$, where c_{s} is the speed of sound, (b) $m^2 > 0$, (c) $\hat{\omega} < N$, and (d) $\lambda_z > Z_{\mathrm{FWHM}}$. We introduce the new variable called wave probability as $p_{\mathrm{GW}} = \frac{N_{\mathrm{GW}}}{N_{\mathrm{MC}}}$ where N_{GW} is the number of samples that fulfill the filter criteria and $N_{\mathrm{MC}} = 10{,}000$ is the number of Monte Carlo samples.

3.3. Spectral Analysis of Temperature Disturbances With Spatial Scales Larger Than the FOV

Figures 2c and 2d reveal large-scale temperature structures exhibiting significant temporal phase progression in both the zonal and meridional directions. These features are assumed to originate from GWs. To extract GW properties as functions of time in a robust and automated fashion, we apply the one-dimensional (1-D) continuous

wavelet transform (CWT), following the methodology described by Ungermann and Reichert (2025). The CWT allows for time-resolved spectral analysis by revealing the frequency content of a signal as it evolves over time (Torrence & Compo, 1998). The AMTM data set comprises a $N_x \times N_y$ array of time series. We compute the 1-D CWT independently for each pixel's time series, resulting in a complex-valued four-dimensional function $\mathrm{CWT}(x, y, t, \omega)$. To assess spatial coherence and phase relationships between adjacent pixels, we calculate the cross wavelet transform (XWT) in the zonal and meridional directions:

$$\mathrm{XWT}_x(x, y, t, \omega) = \langle \mathrm{CWT}(x, y, t, \omega) \cdot \mathrm{CWT}^*(x + \Delta x, y, t, \omega) \rangle \tag{5}$$

$$\mathrm{XWT}_y(x, y, t, \omega) = \langle \mathrm{CWT}(x, y, t, \omega) \cdot \mathrm{CWT}^*(x, y + \Delta y, t, \omega) \rangle, \tag{6}$$

where the asterisk denotes complex conjugation, and angle brackets indicate the inner product (Maraun & Kurths, 2004). The resulting XWT is complex-valued and can be expressed in terms of its amplitude and phase:

$$\mathrm{XWT} = |\mathrm{XWT}| e^{i\Delta\varphi}, \tag{7}$$

where $|\mathrm{XWT}|$ is referred to as the cross wavelet spectrum (XWS), and $\Delta\varphi$ represents the phase difference between neighboring pixels as a function of time and frequency. To focus on wave structures that span the entire FOV and to enhance robustness, we average XWT_x and XWT_y across the FOV. The total cross wavelet spectrum is then computed as $\mathrm{XWS} = 0.5 \cdot (|\mathrm{XWT}_x| + |\mathrm{XWT}_y|)$. Using the known spatial sampling intervals (Δx, Δy), the phase differences are converted to zonal and meridional wavenumbers:

$$(k_x, k_y) = \left(\frac{\Delta\varphi_x}{\Delta x}, \frac{\Delta\varphi_y}{\Delta y} \right). \tag{8}$$

From these, we derive the horizontal wavenumber magnitude and propagation direction:

$$|\boldsymbol{k}| = \sqrt{k_x^2 + k_y^2}, \quad \vartheta = \arctan 2\left(\frac{k_y}{k_x} \right), \tag{9}$$

as well as the horizontal phase speed:

$$\boldsymbol{c} = \boldsymbol{k} \frac{\omega}{|\boldsymbol{k}|^2}. \tag{10}$$

Please note that θ is here defined in the range $[0, \pi)$ ($[0, -\pi)$) anti-clockwise (clockwise) from the positive x-axis. Since we define $\hat{\theta}$ in Equation 2 in the range $[0, 2\pi)$ clockwise from the positive y-axis, we transform θ accordingly.

This analysis yields key GW parameters—amplitude, horizontal wavelength, propagation direction, and phase speed—of waves that are larger than the AMTM's FOV as functions of time and observed frequency.

3.4. Spectral Analysis of Temperature Disturbances With Spatial Scales Smaller Than the FOV

Figures 2e and 2f illustrate small-scale temperature perturbations—defined here as structures with horizontal wavelengths $\lambda_h < 100\,\mathrm{km}$—likely GWs and other features induced by mesoscale processes. Extending the approach introduced in Section 3.3, we aim to retrieve GW properties not only as functions of time but also as functions of space. To this end, we apply a two-dimensional continuous wavelet transform (2-D CWT) to the small-scale temperature perturbation field $T_{\mathrm{small}}(x, y, t)$ at each time step independently. This results in a complex-valued five-dimensional function $\mathrm{CWT}(x, y, t, k_x, k_y)$. To characterize temporal evolution at each spatial and spectral location, we compute the cross wavelet transform in the time domain:

$$\mathrm{XWT}_t(x, y, t, k_x, k_y) = \langle \mathrm{CWT}(x, y, t, k_x, k_y) \cdot \mathrm{CWT}^*(x, y, t + \Delta t, k_x, k_y) \rangle, \tag{11}$$

This approach is analogous to that used by Wright et al. (2021), who analyzed vertical phase differences in AIRS temperature data to infer vertical wavelengths of GWs. The phase-difference method is particularly advantageous for characterizing signals with frequencies too low to be reliably captured by FFT-based techniques. From the phase of $\mathrm{XW}T_t$, we compute the observed frequency:

$$\omega = \frac{\Delta\varphi_t}{\Delta t}. \tag{12}$$

The amplitude of the wave, given by $|\mathrm{XW}T_t|$, is thus a real-valued five-dimensional function of x, y, t, k_x, and k_y. Following the methodology of Hindley et al. (2016), we identify only the dominant wave mode at each point in space and time. This is achieved by iterating over all spatial and temporal positions and selecting the wavenumber pair and associated frequency corresponding to the maximum amplitude. This procedure yields spatially and temporally resolved estimates of the dominant wave's amplitude, horizontal wavelength, propagation direction, observed frequency, and phase speed.

4. Results

Three co-located instruments probed the MLT region above Tierra del Fuego on the night of 21–22 May 2018. The AMTM provides horizontally resolved measurements of temperatures at an altitude of approximately 84 km. Complementary measurements of thermal stratification and background horizontal winds were obtained from CORAL and SAAMER, respectively. Together, these instruments offer a unique data set for investigating MLT dynamics during a period of enhanced GW activity. To characterize the observed wave field, we apply both 1-D and 2-D wavelet analyses, allowing us to quantify GW parameters for features both smaller and larger than the AMTM's FOV. Our MC^2-MF retrieval framework incorporates measurement uncertainties, enabling realistic estimates of GWMF and its associated uncertainty.

4.1. Gravity Waves Smaller Than the AMTM Field of View

MC^2-MF retrieval results from a single AMTM measurement taken at 04:00 UTC on 22 May 2018 are presented in Appendix B to show the retrieval's capabilities. In the following we focus on the overall evolution of GW property distributions. For that matter we compute histograms for every measurement (see Figure 6). The analysis of wave amplitudes (panel a) shows that the most frequently observed values are below 1 K, which is considered to be the noise floor. However, broader distributions containing larger amplitudes up to 5 K emerge during *Vivace* and *Presto*. The wave probability distributions (panel d) vary significantly over time. During *Vivace*, we find narrow distributions close to 100% indicating propagating waves but after 04:00 UTC distributions become broader and a significant fraction points to evanescent modes. A detailed discussion on that matter is provided in Appendix B. A period of reduced wave probability ($p_{\mathrm{GW}} < 50\%$) is noted during *Presto*. To ensure the reliability of further analysis, only waves with amplitudes exceeding 1 K and probabilities above 50% are classified as propagating waves. Only data that fulfills these criteria is illustrated in panels b, c, and e-x. During *Vivace* horizontal wavelengths (panel b) consistently exceed 20 km. Eye-catching is a distinctive "peak-streak" pattern observed from 02:30 UTC ($\lambda_{\mathrm{h}} \approx 50$ km) to 04:00 UTC ($\lambda_{\mathrm{h}} \approx 80$ km) which might be connected to a larger-scale structure appearing after 04:00 UTC. During *Presto* we observe GWs with $\lambda_{\mathrm{h}} = 60-90$ km. Vertical wavelengths (panel c) are first in the range 20–30 km but increase toward 50 km after 04:00 UTC. This is the time of strongest horizontal winds (see Figure 4). Vertical wavelengths shrink below 20 km as times approach *Presto* and increase again toward 20 km after that. Between 01:00 UTC and 07:00 UTC, distributions of observed phase speed (panels f–k) focus in the west-northwest-sector with $|\boldsymbol{c}| < 20\,\mathrm{m\,s^{-1}}$. We follow Taylor et al. (1993) and construct blocking diagrams based on JAWARA wind profiles from the surface to 84 km (see Figures 6e–6n). These diagrams estimate the phase speeds and propagation directions accessible to surface-generated GWs. Please note that between 01:00 UTC and 07:00 UTC the peak of the phase speed distribution is always outside the blocking area. At the same time, we observe MFs of up to $20\,\mathrm{m^2\,s^{-2}}$ (panels q–t) in westward direction. During *Presto* (panel l, m), we find additional phase speeds of up to $70\,\mathrm{m\,s^{-1}}$ in southeast-direction while westward oriented phase speeds disappear. This is accompanied by southeast- and northeast-oriented MFs (panels v, w). On average relative uncertainties are 8% for $\hat{\omega}$, 61% for λ_z, and 50% for MF at one specific pixel in the temperature maps. These values are in agreement with results from previous studies such as Fritts et al. (2014) and Vargas (2019).

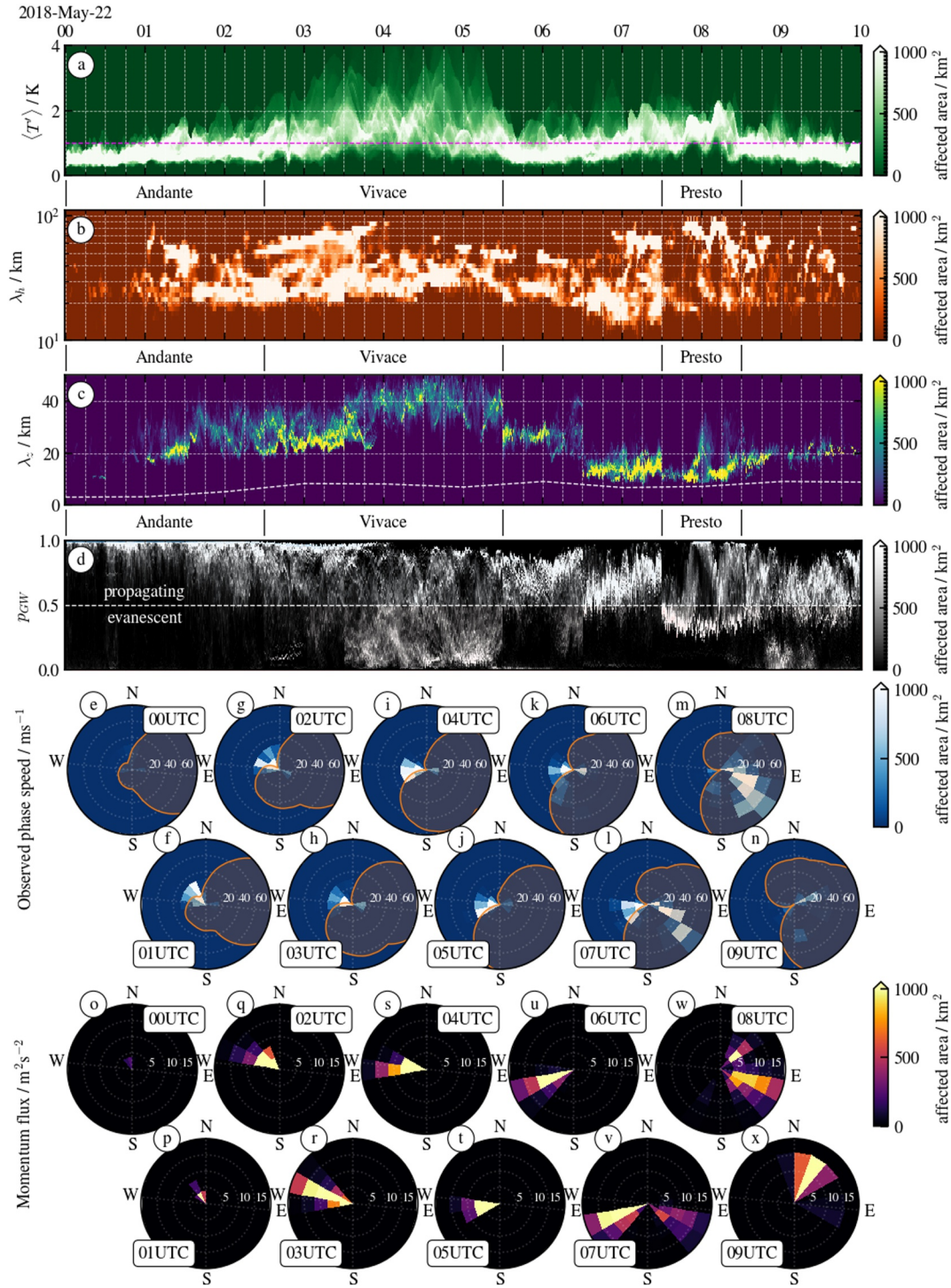

Figure 6. Time–histogram overview of GW properties retrieved from 1,045 consecutive AMT maps. Panels: (a) temperature-perturbation amplitude; the magenta line indicates the 1 K noise floor. (b) Horizontal wavelength. (c) Vertical wavelength; the white line denotes the derived OH*(3-1) layer thickness. (d) Probability that a given pixel contains a propagating wave. (e–n) Histograms of observed phase speed; the orange contoured area marks blocked phase speeds based on JAWARA wind profiles for surface-generated GWs. (o–x) Histograms of momentum flux. Since histograms reflect pixel counting, units are given in km^2.

When computing FOV-averages and assuming statistical independence, uncertainty values can be reduced significantly.

4.2. Gravity Waves Larger Than the AMTM Field of View

Figure 7 presents FOV-averaged wave properties, including amplitudes, horizontal wavelengths, observed phase speeds, vertical wavelengths, and MFs. As in Section 4.1 we discard MF estimates and vertical wavelengths where the probability of a propagating wave solution falls below 50%. In addition, we focus on wave properties inside the cone of influence since outside edge effects render the wavelet analysis unreliable (Torrence & Compo, 1998).

During *Vivace* we notice a region of $\langle \hat{T} \rangle$ exceeding 1 K with observed periods larger than 1 hr, $\lambda_h = 100-400$ km, and observed phase speeds up to 100 ms^{-1} propagating first northwestward and then turning westward. A peak MF of 1.3 m^2 s^{-2} coincides with smallest vertical wavelengths ($\lambda_z \approx 20$ km) at the onset of the *Vivace* phase. The occurrence of this warm phase front in the AMTM measurements coincides with enhanced temperatures as seen in the CORAL measurements (see Figure 3a). In these we find a downward migration of the warm phase front—a motion the OH*(3-1) layer seems to follow (see Appendix A)—which indicates an overall upward propagation of this GW. Between *Vivace* and *Presto* we find another peak in temperature amplitude exceeding 2 K exhibiting a relatively modest MF of 0.9 m^2 s^{-2} due to long horizontal wavelengths ($\lambda_h > 600$ km). This wave propagates predominantly eastward with rather large phase speeds exceeding even 200 ms^{-1}. The *Presto* stage is characterized by a fast southeastward propagating GW with $|\boldsymbol{c}| = 94 \pm 12$ ms^{-1}, $\langle \hat{T} \rangle = 1.7$ K, $\hat{T} = 2.0$ K, $\omega = 3.4 \cdot 10^{-3}$ s^{-1}, $\lambda_h = 173$ km, $\lambda_z = 31$ km, and $|\boldsymbol{F}| = 2.1 \pm 1.3$ m^{2}s^{-2}. This *Presto* wave packet is identified as two wave cycles in the keograms (see Figures 2c and 2d) and a band intensity snapshot of this wave packet is depicted in Figure 1b.

5. Discussion

In the following paragraphs, we discuss results and derived uncertainties from our newly developed MC^2-MF retrieval and investigate the physical mechanisms underlying *Andante*, *Vivace*, and *Presto* addressing the central questions of this study: Did we observe 2GWs in the MLT above Tierra del Fuego?

5.1. The MC^2-MF Retrieval

Our MC^2-MF retrieval is not the first to combine co-located airglow-lidar-MR observations but it is the first that does so in a routine fashion. In addition, it is also the first time that the imprecise knowledge of the OH*(3-1) layer peak altitude and thickness are realistically reflected in the uncertainties of the static stability and the background wind in the frame work of the MC^2-MF retrieval. Earlier studies (e.g., Fritts et al., 2014; Pautet et al., 2021; Reichert et al., 2019) have either used climatological values for Z_{peak} and Z_{FWHM} or an OH*(3-1) concentration profile snapshot from SABER but neglected any temporal variability. Hence, uncertainties in N were rather small: Pautet et al. (2021) assumed 10% uncertainty based on climatology; Vargas (2019) reported 8% from seasonal data from a location about 24° north of our measurement site; and Fritts et al. (2014) achieved 5–6% using sodium lidar measurements. However, these works did not account for OH*(3-1) layer variability, which—combined with increasing lidar measurement noise—explains a higher N uncertainty of 25% in our study. A short discussion on detailed results of our MC^2-MF retrieval are provided in Appendix B.

5.2. *Vivace*: Observational Evidence for Mountain Waves

When sufficiently strong winds interact with the complex orography of Patagonia, MWs are excited and propagate vertically into the middle atmosphere (e.g., Alexander & Teitelbaum, 2011; de la Torre et al., 2012; Fritts et al., 2021; Krasauskas et al., 2023; Lund et al., 2020; Pautet et al., 2021; Rapp et al., 2021; Reichert et al., 2021). On the night of 21–22 May 2018, a westerly flow of 10 − 15 ms^{-1} at 700 hPa impinged upon the southern Andes mountain ridge, extending from roughly 40°S to the southern tip of the continent. Under such synoptic forcing, the excitation of MWs along the southern cordillera is expected (e.g., Dörnbrack et al., 2002; B. Kaifler et al., 2015; Bramberger et al., 2017). At 10 hPa, the core of the Polar Night Jet (PNJ) was located above the Drake Passage, favoring lateral (southward) propagation of large-scale MWs into the PNJ (e.g., Ehard et al., 2017; Sato et al., 2012). Under similar conditions, Kogure et al. (2020) observed concentric ring-like structures in the OH*(3-

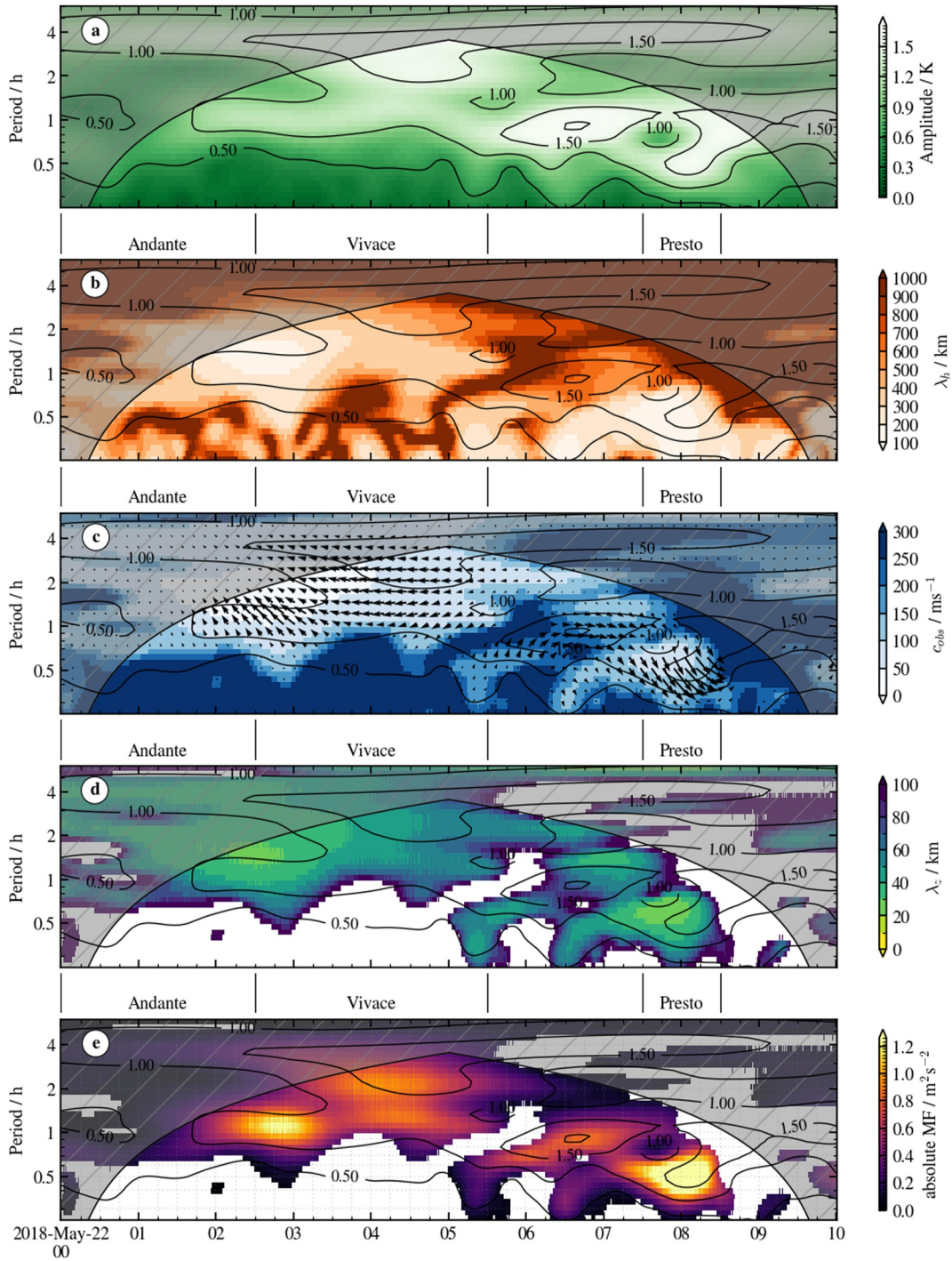

Figure 7. (a) FOV average temperature amplitude of T_{large}, (b) Horizontal wavelength, (c) Observed phase speed (arrows mark the propagation direction), (d) Vertical wavelength derived from dispersion relation, (e) Momentum flux. Contours refer to amplitudes from panel (a), gray hatched area marks the cone of influence and white out areas are due to non-propagating wave solutions.

1) layer leeward of the southern Andes and concluded that these are 2GWs generated by the breaking of leeward propagating MWs.

Temperature perturbation fields from the Integrated Forecast System (IFS (Wedi et al., 2015);) of the European Centre for Medium-Range Weather Forecasts reveal vertically coherent, stationary phase lines with amplitudes

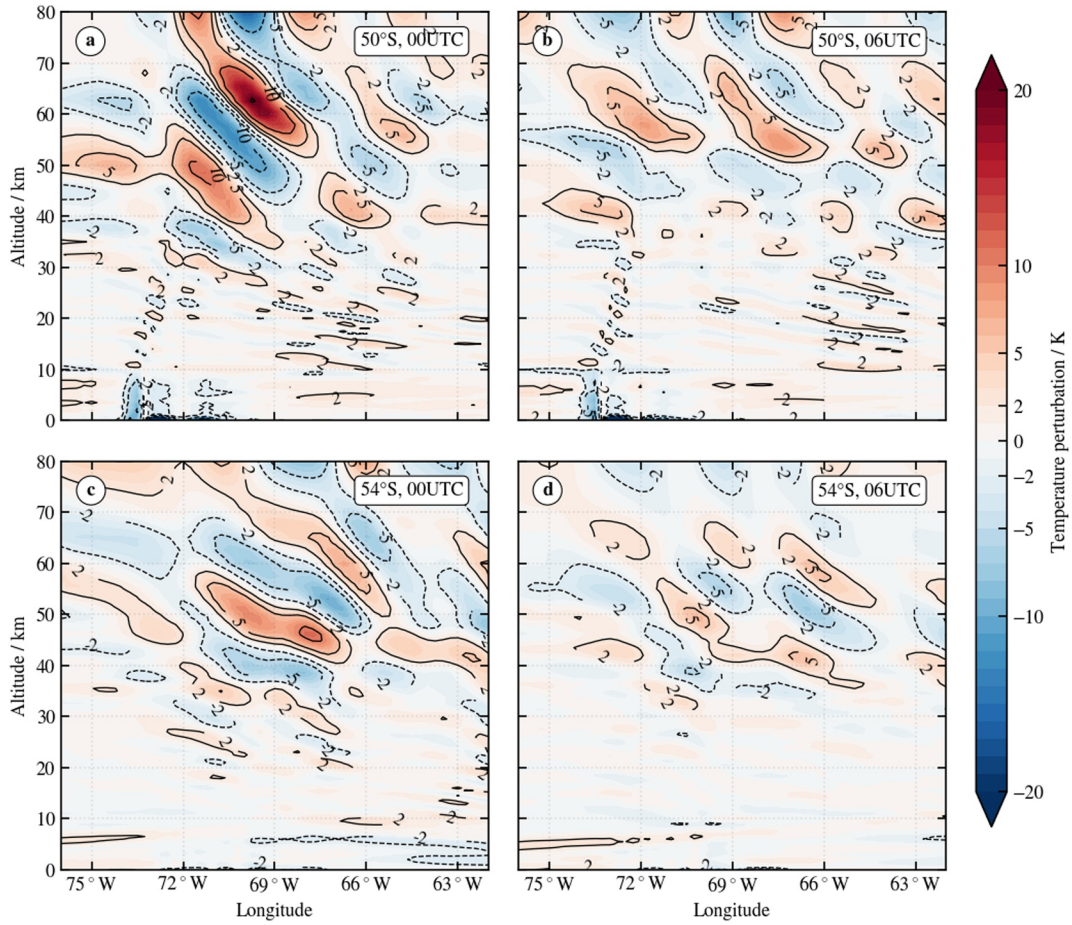

Figure 8. Longitude-altitude cross sections of temperature perturbation fields taken from IFS at 50°S, 00 UTC (a), 50°S, 06 UTC (b), 54°S, 00 UTC, and 54°S, 06 UTC (d).

up to 20 K above the stratopause (see Figure 8). Their alignment, vertical extent, and position over orography support interpretation as MWs. IFS data further suggest that MW amplitudes at 54°S (within 0.3° to the observation site latitude) are approximately half of those at 50°S, and similarly reduced by a factor of two 6 hours later, indicating temporal and latitudinal weakening of MW activity.

Wind profiles from the JAWARA reanalysis show strong westerlies up to 70 km (see Figure 5), above which wind speeds decrease sharply, forming a strong shear layer with Richardson numbers as low as 0.25. This region of dynamic instability may favor the development of Kelvin–Helmholtz instabilities and shear-induced GWs (e.g., Fritts, 1982; Hecht et al., 2001; Kjellstrand et al., 2022; Yasui et al., 2018). If such waves formed and were stationary relative to the shear zone, they could manifest as quasi-stationary phase lines in temperature maps. Since the shear zone is embedded in a background wind that strengthens from 10 ms^{-1} at 03:00 UTC to 60 ms^{-1} at 06:00 UTC, however, these GWs generated by shear would be observed as accelerating structures in our ground-based observations. However, histograms of observed phase speed indicate no acceleration but show narrow distributions ranging from 0 ms^{-1} to 20 ms^{-1}. Additionally, an arc-shaped structure is observed at 04:00 UTC (see Figure 1a), similar to features reported over Auckland Island during the DEEPWAVE campaign (Mixa et al., 2021; Pautet et al., 2016). This reflects a localized orographic feature, likely the elevated terrain near Mt. Darwin. The last two pieces of evidence contradict a shear generation mechanism.

The IFS model, with a horizontal resolution of 9 km, resolves GWs with horizontal wavelengths larger than ~50 km. Therefore, while it may capture enhanced MW activity at the correct time and geolocation, smaller-scale structures—such as the observed wavelengths of as short as 20 km—remain unresolved. We need other diagnostics to investigate whether short-scale MWs are able to propagate to OH*(3-1) emission layer altitudes. The blocking diagrams (see Figures 6e–6n) show that only during the 03:00–08:00 UTC period, zero-phase-speed (i.

e., MW) modes are able to reach the OH*(3-1) layer. During *Andante*, MWs find a critical level at 70 km prohibiting their vertical propagation. *Vivace* coincides with the westerly phase of the semi-diurnal tide in which the detected occurrence rate of MWs is generally enhanced (Pautet et al., 2021). This is due to longer vertical wavelengths and therefore less phase averaging which improves the detection of GWs in OH*(3-1) emission observations. In addition, even though there is no critical level below, the majority of MWs disappear after *Vivace* because ambient winds weaken and so the vertical wavelength shrinks and phase averaging makes MWs invisible for the AMTM. The preferred propagation direction of MWs during *Vivace* shifts from northwesterly at 03:00 UTC to westerly by 08:00 UTC. Following the MW propagation direction, we compute the Scorer parameter (Scorer, 1951) according to

$$l^2 = \frac{N^2}{u_{\parallel}^2} - \frac{1}{u_{\parallel}} \frac{d^2 u_{\parallel}}{dz^2}, \tag{13}$$

where the Scorer wavelength $\lambda_{Sc} = 2\pi/l$ defines the minimum horizontal wavelength required for MWs to avoid reflection. N and $u_{\parallel}$ for λ_{Sc} are taken from JAWARA reanalysis. During *Vivace*, λ_{Sc} is on the order of 20–25 km—closely matching the horizontal wavelengths found in our 2-D wavelet analysis of temperature maps (see Figure 6b). Since we find a small fraction of GWs with scales smaller than λ_{Sc} we conclude that this part of the spectrum must have tunneled through the PNJ (Mixa et al., 2021).

Pautet et al. (2021) report that GWMF could only be derived in 36 out of 97 MW cases due to indeterminate or too-small vertical wavelengths. The night of 21–22 May 2018 falls into this category. Indeed, using mean stratification and mean wind yields a complex vertical wavenumber and intrinsic frequency $\hat{\omega} > N$, indicating evanescence. Our novel MC^2-MF retrieval, however, provides distributions of intrinsic GW properties and allows for the separate investigation of conditions for propagating and evanescent modes. In the detailed analysis of the MC^2-MF retrieval results (see Appendix B) we notice a spatial relationship of p_{GW}, T_{large}, λ_h, $\hat{\omega}$, N, and u'. We conclude that the larger-scale westward and upward propagating GW that we observe in the AMTM measurements (see Figure 2c) and in the CORAL measurements (see Figure 3a) alters atmospheric background conditions such that short-scale MWs are able to propagate into higher altitudes. Due to the coarse spatial resolution of SAAMER the localized effect of the larger-scale GW on winds and vertical wind shear is not detected. These results suggest that interaction of large- and small-scale GWs has contributed to a number of MW cases in Pautet et al. (2021) where the vertical wavelength was indeterminate or too small.

Another indication on the vertical propagation of these small-scale GWs is provided by co-located airglow measurements of Sodium (~90 km) and Oxygen (~96 km) (see Figures S3 and S4 in Supporting Information S1). Band intensity maps close to 04:00 UTC show wave structures with wavelengths in the same order as in the AMTM measurements. Since these structures are quasi-stationary as well, their interpretation as MWs agrees well with westerly winds as measured by SAAMER at 90 and 96 km.

We conclude that the small-scale structures are indeed vertically propagating MWs. Additional support for the presence of MWs during *Vivace* comes from CORAL lidar temperature observations, which display quasi-stationary phase lines with alternating regions of enhanced stratification and convective instability. This indicates not only MW presence but also their breaking above the stratopause—a hallmark of momentum deposition and a potential source of 2GWs (Vadas et al., 2018).

The critical level for MWs at 73 km during *Andante* becomes a wind minimum during *Vivace* and is considered a valve layer (Kruse et al., 2016). This mesospheric valve below the OH*(3-1) layer explains relatively small GWMF in the order of 10 m^2 s^{-2}. Such values are not only realistic since Pautet et al. (2021) have shown that MW momentum fluxes are mostly below 100 m^2 s^{-2} but also rather small since they found an average value of ~250 m^2 s^{-2}.

5.3. *Presto*: Observational Evidence for Secondary Gravity Waves

During the *Presto* interval a rapidly propagating ($|\hat{c}| = 94$ ms^{-1}) large-scale ($\lambda_h = 173$ km) GW packet is observed in the OH*(3-1) emission layer above Tierra del Fuego. It transports a peak GWMF of 2.1 m^2 s^{-2} in a southeastward direction. In addition, we find medium-scale ($\lambda_h \approx 50-80$ km) fast ($\hat{c} \approx 70$ ms^{-1}) GWs carrying

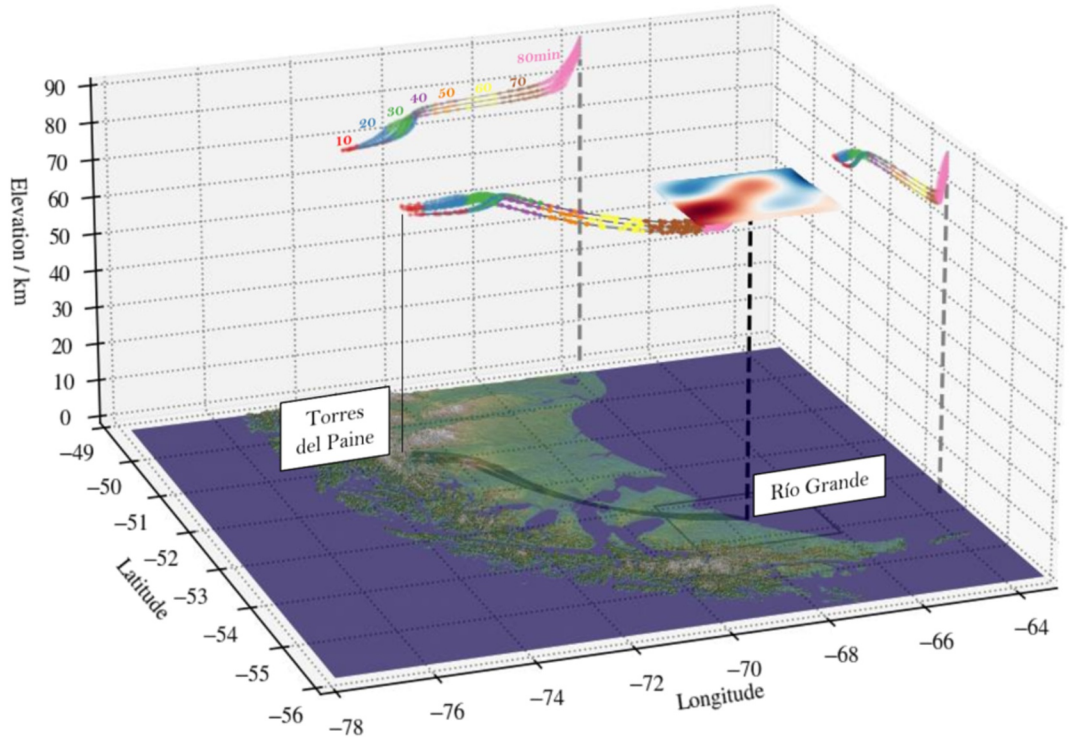

Figure 9. Backwards trajectories of the *Presto* wave packet using GROGRAT. JAWARA reanalysis is used as background atmosphere. Colors indicate propagation time in minutes. Projections of trajectories are shown on longitude-altitude plane and latitude-altitude plane.

up to 20 $m^2 s^{-2}$ MF propagating in the same direction as their larger-scale counterparts. We argue that our separation of AMTM temperatures in T_{small} and T_{large} leads to the appearance of the same wave packet in the analysis of GWs both smaller and larger than the AMTM's FOV. To determine whether this packet represents a 2GW produced by local body forces from breaking MWs rather than a wave generated in situ in the mesospheric shear zone, we examine its dynamical context, origin, and consistency with theory. Synoptic analyses and the results discussed in Section 5.2 demonstrate vigorous MW activity extending at least ∼500 km northwest of Tierra del Fuego under uniform westerly forcing of 10−15 ms^{-1} at 700 hPa. CORAL temperature profiles over Río Grande reveal layers of convective instability in the ranges 58–66 km and 72–82 km, indicative of MW breaking and momentum deposition in these altitudes. The latter convectively unstable layer coincides with a critical level for MWs during *Andante*. With similar forcing and propagation conditions and enhanced MW activity according to the IFS, it is very likely to find GW breaking due to convective instability, hence local body forces that are capable to generate 2GWs, in similar altitudes further northwest. Assuming similarly rough terrain at Tierra del Fuego and farther Northwest along the Andes mountain ridge, we expect a comparable MW source spectrum. Using the spectral parameters retrieved for the large-scale *Presto* wave packet, backward raytracing with the Gravity-wave Regional Or Global Ray Tracer (GROGRAT) (Eckermann, 1992; Marks & Eckermann, 1995) and JAWARA reanalysis links the packet to a source region near (51°S, 73°W) at roughly 63 km altitude (see Figure 9). These results indicate a source region for the *Presto* wave packet over the Torres del Paine massif.

Sensitivity tests show that adjustments to the stratification shift the source altitude upward but leave the coordinates of the source unchanged, supporting this location as the launch site. We have illustrated the trajectories in the geographical context in Figure 9. Due to its high phase speed, the *Presto* wave packet propagated from the Torres del Paine massif to Tierra del Fuego within only about 80 min. Variable wind speeds and stratification result in a step-like ascent of the wave packet.

If the *Presto* wave packet was generated at 63 km above Torres del Paine by breaking MWs, why do we observe it only in this short time frame? To answer that, we use JAWARA reanalysis to compute the vertical wavelength (see Equation 4) of the *Presto* wave packet over Tierra del Fuego as function of time and altitude and to calculate forward GROGRAT trajectories of the wave packet at earlier times (see Figure 10). It becomes clear that a turning

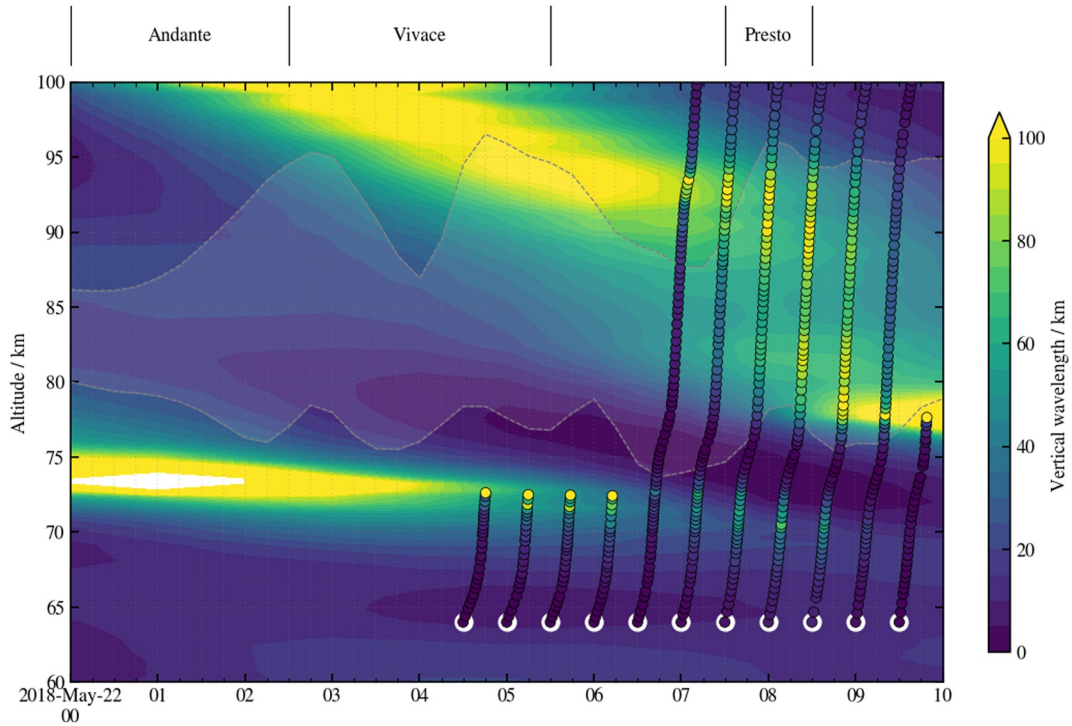

Figure 10. Vertical wavelength of the 2GW as function of time and altitude computed from Equation 4 using JAWARA reanalysis. Colored circles are GROGRAT results. Opaque region between dashed lines marks derived OH*(3-1) layer.

level below the OH*(3-1) layer (73–75 km) leads to the reflection of the *Presto* wave packet before 06:30 UTC and after 09:30 UTC. Only within ±30 min of the time frame of *Presto*, atmospheric background conditions allow for the vertical propagation of the wave packet. If the *Presto* wave packet would have been generated at the critical level for MWs (73 km) or would be shear generated, we would observe this wave throughout the night in the airglow layer. However, given the limited wave detection during *Presto* as well as the presence of a turning level, we conclude that the *Presto* wave packet was generated below 73 km and therefore stems from MW breaking likely due to convective instabilities at 63 km. This defines the *Presto* wave packet as a 2GW.

Our interpretation is reconfirmed by the CORAL observation. Enhanced wave amplitudes are only found between ∼76 − 82 km (see Figure 3c). The upper boundary is likely due to enhanced noise levels while the lower boundary indicates that the 2GW enters CORAL's FOV here and is therefore horizontally propagating. This picture changes after ∼09:00 UTC where amplitudes shift downwards indicating that a newly developed turning level at 77–79 km that keeps 2GW activity at lower levels. Our interpretation aligns with established theory: momentum deposition by breaking primary MWs acts as a localized body force that radiates 2GWs into the upper atmosphere (Becker & Vadas, 2020; Vadas & Becker, 2019). The 2GW's 173 km horizontal wavelength is roughly eight times longer than the 20–25 km wavelength of the MWs observed four hours earlier—a scaling consistent with numerical predictions and prior observations of 2GWs (Vadas et al., 2018). On the other hand, Kogure et al. (2020) linked the generation of 2GWs with horizontal wavelengths in the order of 100 km to MWs with horizontal wavelengths in the order of 500 km. Since the IFS also shows large-scale MW activity in the vicinity of Torres del Paine, we cannot exclude the possibility that those larger-scale MWs are responsible for the excitation of the observed 2GW.

We note that the observed phase speed of the 2GW is similar to the speed of mesospheric bores (e.g., Dewan & Picard, 2001; Smith et al., 2003; Yue et al., 2010). Typically, a mesospheric bore is observed as a jump-like disturbance in airglow brightness followed by a number of smaller-scale trailing waves within a waveguide (e.g., thermal duct). Indeed, we observe a thermal duct between 78 and 90 km, but instead of a sharp leading front and trailing waves, we rather observe two large-scale wave cycles. Due to increasing noise levels, we cannot prove whether the 2GW is confined to the altitude region of the thermal duct, nor do we have additional Na- and OI-airglow observations during *Presto* due to technical issues.

Taken together—uniform MW forcing upstream, convective instability at 58–66 km, raytracing convergence over Torres del Paine at ∼63 km, the absence of continuous wave activity expected from shear-generated waves, and the wavelength scaling—the evidence strongly supports the interpretation that the fast GW observed during *Presto* is a 2GW generated by momentum deposition of breaking MWs over the Torres del Paine massif rather than a wave produced in situ in the mesospheric shear zone.

6. Summary and Conclusion

On the night of 21–22 May 2018 the AMTM recorded temperature maps from the MLT above Tierra del Fuego and detected GWs of different spatial and temporal scales. These measurements were complemented by CORAL Rayleigh lidar temperature soundings in the middle atmosphere and SAAMER MR wind observations in the MLT. This rare combination of co-located measurements enabled the retrieval of intrinsic GW parameters and MF, as demonstrated in previous studies (e.g., Fritts et al., 2014; Reichert et al., 2019). In a two-stage Monte Carlo simulation (MC^2) we account for uncertainties from the OH*(3-1) layer peak altitude and thickness as well as from temperature and wind measurements to obtain appropriate distributions of intrinsic GW properties. The observed spectral properties are derived using 1-D (2-D) wavelet analysis (Ungermann & Reichert, 2025) for GWs larger (smaller) than the AMTM's FOV. We summarize our methodology:

- The OH*(3-1) layer peak altitude and thickness is estimated as function of time relating height-weighted Rayleigh lidar temperatures with AMTM temperatures. Additional uncertainties are based on CORAL measurement errors. The temporal evolution of OH*(3-1) layer properties shows not only smooth migration with tides or long-period GWs but also jumps potentially due to processes where vertical mixing is involved. Uncertainties are likely underestimated due to the assumption of a Gaussian shaped OH concentration profile.
- The 2-D XWT is a suitable tool to analyze temperature maps with regard to GW structures that are smaller than the AMTM's FOV and explicitly quasi-stationary MW structures. Even though computationally more expensive than the usual FFT algorithm, it enables spatiotemporal tracking of dominant wave parameters. Similar to the 2D + 1 ST used by Wright et al. (2017) the spectral component in the third dimension is retrieved via phase shift. Since subsequent temperature maps are analyzed, this approach also mitigates contamination by allowing exclusion of cloud compromised images—something not possible in traditional time series analysis. Notably, this marks the first application of this technique to MLT temperature maps. We acknowledge that wave amplitudes are likely underestimated due to spectral leakage.
- In the absence of significant cloud contamination we applied 1-D XWT to AMTM timeseries and derived FOV averaged wave parameters as function of time and observed period. As in the 2-D case, horizontal wavenumbers k and l are derived via a phase shift in the zonal and meridional direction, respectively. This approach enables the analysis of GWs larger than the FOV and is more straightforward than fitting linear functions to phase lines as done by Reichert et al. (2019).
- We developed a MC^2-MF retrieval that takes into account uncertainties in OH*(3-1) layer peak altitude and thickness as well as measurement uncertainties of stratification and horizontal wind which yields appropriate distributions of intrinsic GW parameters. Given enhanced uncertainties in atmospheric background variables we argue that it is essential to propagate errors via our computationally more expensive MC^2 approach and not via standard Gaussian error propagation. Retrieved results allow for a better interpretation of the physical processes.
- Dealing with distributions rather than mean values, we were able to identify an interaction between a larger scale GW that seemed to have altered atmospheric background conditions such that the smaller-scale MWs were able to propagate into higher altitudes. We speculate that more of these wave-wave-interactions are the reason why Pautet et al. (2021) had to discard almost two thirds of MW cases due to indeterminate or too small vertical wavelengths.

The combined airglow-lidar-MR observation detected first quasi-stationary small-scale ($\lambda_h = 20-40$ km) and fast propagating ($|\hat{c}| = 94\,\mathrm{ms}^{-1}$) large-scale ($\lambda_h \approx 170$ km) GWs a few hours later in the MLT above Tierra del Fuego. Initially, we asked if these two types of waves were MWs and 2GWs reflecting the process of multi-step vertical coupling. We are aware though that the MWs observed over Tierra del Fuego cannot have generated the observed large-scale 2GWs since their source is presumably 500 km away. For our conclusion, we focus our attention on two key regions: (a) Torres del Paine and (b) Tierra del Fuego. We summarize our findings in these two regions:

- Favorable conditions existed for MW excitation throughout the measurement period, driven by westerly flow from 40°S to the southern tip of South America including Torres del Paine and Tierra del Fuego. Small-scale MWs propagated merely vertically into the middle atmosphere directly above Torres del Paine and Tierra del Fuego. A critical level at 73 km initially inhibited any further vertical propagation, but later developed into a mesospheric valve layer allowing MWs to reach the OH*(3-1) airglow emission layer above Tierra del Fuego. Retrieved GWMF are always smaller than 20 $m^2 s^{-2}$. In the absence of measurements over Torres del Paine, we infer similar processes due to comparable orographic forcing and background winds.
- CORAL temperature profiles show a region of convective instability at 58–66 km indicating momentum deposition below the critical level at 73 km and hence potential generation of 2GWs. IFS data suggest even stronger MW activity over Torres del Paine, supporting the assumption of analogous dynamics.
- GROGRAT backward trajectories of 2GWs cross the Torres del Paine region at an altitude of 63 km, which is in line with the region of convective instability in these altitudes over Tierra del Fuego.
- 2GWs are assumed to be generated throughout the night at ∼63 km over Torres del Paine but encountered a turning level at 73–75 km within the first few hours of the measurement night, which is the reason why they were not detected over Tierra del Fuego first. As the barrier weakened, 2GWs reached the OH*(3-1) layer and became visible in AMTM observations. Their peak MF is estimated to 2.1 $m^2 s^{-2}$.

By analyzing a single-night case study we implement the automated, multi-instrument GW analysis envisioned by Fritts et al. (2014). Our new MC^2–MF algorithm combines 1-D and 2-D XWT to retrieve intrinsic GW parameters and GWMF from the full airglow–lidar–MR data set without requiring subjective selection of visually striking features. The next step is to apply this framework to a full year of co-located observations over Tierra del Fuego. The resulting climatology of mesospheric GW properties and GWMF will be compared with the MW statistics of Pautet et al. (2021), who demonstrated that MW occurrence peaks during the westerly phase of the semi-diurnal tide. Extending the analysis to all wave scales raises several open questions: (a) How do migrating and non-migrating tides modulate the propagation and dissipation of MWs across different horizontal scales and vertical phase speeds? (b) Is the generation of 2GWs tied to local time through tidal control of breaking altitudes? (c) To what extent do tides modify the filtering of 2GWs as they ascend into the upper mesosphere and lower thermosphere? Addressing these issues will require both expanded observational statistics and targeted, idealized numerical simulations capable of separating tidal, orographic, and nonlinear GW-interaction effects.

Appendix A: Estimation of OH*(3-1) Layer Peak Altitude Z_{peak} and Thickness Z_{FWHM}

The AMTM provides temperature measurements representing a weighted average over the OH*(3-1) layer temperature distribution (Fritts et al., 2014; Pautet et al., 2014). Rocket measurements by Baker and Stair (1988) report an OH*(3-1) layer peak altitude of $Z_{peak} = 86.8 \pm 2.6$ km and a full-width at half-maximum (FWHM) of $Z_{FWHM} = 8.6 \pm 3.1$ km. A Gaussian fit to the OH 1.6 µm concentration profile from SABER data on 22 May 2018 at 06:16 UTC (Figure S1 in Supporting Information S1) yields a peak altitude of 85.8 km and a thickness of 9.3 km, consistent with Baker and Stair (1988). However, the SABER profile's tangent point at 51.3°S, 61.2°W, located over 500 km northeast of Río Grande during SABER's northern yaw cycle, may not accurately represent local OH concentrations. Additionally, temporal variations in OH*(3-1) layer peak altitude and thickness remain unknown. To address this, we estimate the temporal evolution of Z_{peak} and Z_{FWHM} by comparing CORAL lidar and AMTM temperature time series. Following the method of Zhao et al. (2005), who determined the OH*(3-1) layer peak altitude above Maui, Hawaii, by convolving Na-lidar temperature profiles with a Gaussian of fixed standard deviation and identifying the altitude minimizing the absolute difference with mesospheric temperature mapper (MTM) data, we extend this approach by allowing the Gaussian standard deviation to vary. This enables estimation of both the OH*(3-1) layer peak altitude and thickness as functions of time. We first utilize CORAL photon counts from a reference altitude of 40 km with a temporal resolution of 10 s to exclude AMTM temperature data from the analysis where photon counts are below 25% of the photon counts median. By doing so, we exclude cloud contaminated AMTM temperatures from the analysis. In the estimation of Z_{peak} and Z_{FWHM} we utilize CORAL lidar temperature data with a temporal resolution of 60 min (binned to 15 min) for three key advantages: (a) extended integration allows retrieval of temperature profiles up to 95 km, improving overlap with the OH*(3-1) layer; (b) reduced temperature uncertainties due to longer integration; and (c) focus on correlation with large-period temperature variations, as the OH*(3-1) layer is assumed to respond primarily to low-frequency perturbations such as tides and long-period GWs. The AMTM temperatures are averaged over the 4 × 4 pixel region

centered at the lidar spot. In this average, the 3 × 3 pixel region that is contaminated by the lidar spot itself is excluded. The resulting temperature time series is binned to 15 min averages for consistency with the lidar temperatures. The weighting is performed with normal distributions spanning peak altitudes from 79 to 95 km and thicknesses from 3 to 14 km, encompassing three standard deviations based on Baker and Stair (1988).

In the following we describe step by step how we estimate the OH*(3-1) layer peak altitude and thickness.

1. *Define initial coordinates in the search for cost-function minimum*
   Initialize coordinates in the parameter space. We start here with climatological values, that is $Z_{\text{peak}} = 86.8$ km and $Z_{\text{FWHM}} = 8.6$ km. The algorithm starts at these coordinates to search for the closest minimum of the cost-function (defined in step 5 of the algorithm). Generally, the cost-function has more than one minimum. Hence, the initial coordinates may be critical in the determination of the minimum.
2. *Iterate over time and parameter space*
   The cost-function is computed as function of Z_{peak} and Z_{FWHM} and for each time step independently.
3. *Compute Gaussian weighted lidar temperature*
   Lidar temperatures are weighted with a normal distribution according to

$$T_{\text{lidar-OH}} = \sum_i T(z_i)\, w_i(Z_{\text{peak}}, Z_{\text{FWHM}}) \tag{A1}$$

$$\Delta T_{\text{lidar-OH}} = \sqrt{\sum_i \left(\Delta T(z_i) w_i(Z_{\text{peak}}, Z_{\text{FWHM}})\right)^2} \tag{A2}$$

   where $w(Z_{\text{peak}}, Z_{\text{FWHM}}) = \frac{1}{\sqrt{2\pi\sigma^2}} e^{-\frac{(z-Z_{\text{peak}})^2}{2\sigma^2}}$ and $\sigma = \frac{Z_{\text{FWHM}}}{2.355}$.
4. *Compute the cost-function*
   Compute the absolute difference between the AMTM and the Gaussian weighted CORAL temperature.
5. *Find the closest minimum*
   Start at the initial coordinates defined in step 1 and find the closest minimum of the cost-function.
6. *Define the neighborhood*
   Compute the relative temperature difference according to

$$dT_{rel} = \frac{|T_{\text{AMTM}} - T_{\text{lidar-OH}}| - \text{Min}(|T_{\text{AMTM}} - T_{\text{lidar-OH}}|)}{\Delta T_{\text{lidar-OH}}} \tag{A3}$$

   and find the neighborhood of the minimum where $dT_{\text{rel}} < 1$. This neighborhood distinguishes itself as the number of $(Z_{\text{peak}}, Z_{\text{FWHM}})$-pairs that are reachable from the minimum within the temperature uncertainty range.
7. *Estimate* OH*(3-1) *layer peak altitude and thickness*
   The center of gravity of the neighborhood corresponds to the peak altitude and thickness of the OH-layer. The standard deviation of the neighborhood provides an estimate of the uncertainty of the OH*(3-1) layer's peak altitude and FWHM.
8. *Update initial coordinates*
   The derived values for the OH*(3-1) layer's peak altitude and thickness are filtered with a median filter of window size three in order to construct temporal consistency. After that, the initial coordinates from step 1 are updated with the median-filtered values of the OH*(3-1) layer peak altitude and thickness.
9. *Compute Correlation, RMSE, and bias*
   When steps 1–8 are done three times, we construct a time series $T_{\text{lidar-OH}}(t)$ (Figure A1a) and compute the correlation (Figure A1d), RMSE (Figure A1b) and mean temperature difference (Figure A1c), that is bias, with the AMTM temperature time series.
10. *Perform bias correction*
    Generally, the AMTM and CORAL temperatures can show a constant bias in the MLT since CORAL temperatures are seeded with temperatures from SABER which was in the northern yaw-cycle by that time and therefore, the profile is approx. 500 km away from Río Grande. In order to account for that bias, we subtract the bias from the CORAL temperatures and repeat the whole procedure until the cumulative bias is below 0.05 K which is the Gaussian weighted nightly mean temperature uncertainty.

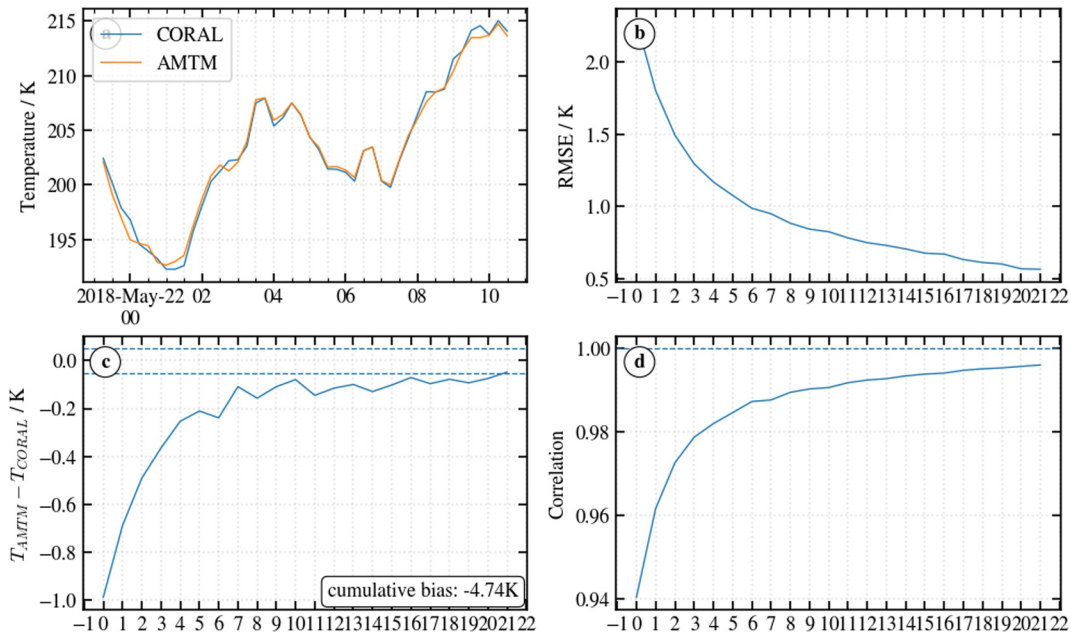

Figure A1. Weighted lidar temperature (blue) and AMTM temperature (orange) (a), RMSE as function of iteration (b), Mean temperature deviation as function of iteration (c), and Correlation as function of iteration (d).

The temporal evolution of $(Z_{\text{peak}}, Z_{\text{fwhm}})$ is shown in Figure S2 in Supporting Information S1. Notable are abrupt transitions, likely artifacts from the assumption of Gaussian-shaped OH concentration profiles. To mitigate this, we apply a Gaussian filter to smooth the $(Z_{\text{peak}}, Z_{\text{fwhm}})$ time series, subsequently using the smoothed values for OH*(3-1) layer weighted static stability and wind estimations.

Appendix B: Results of the MC^2-MF Retrieval at One Single Time Step

In Figure B1 we provide detailed insights into our MC^2-MF retrieval at one representative time step: 22 May 2018 at 04:00 UTC. This time falls within the previously defined *Andante* period during which MWs are observed. Panels (a) and (b) display the small-scale temperature perturbations $T_{\text{small}} + T_{\text{noise}}$ and the background temperature T_0, respectively, as defined in Section 2.1. We notice small-scale wave structures oriented north-south, whereas T_0 reveals a larger-scale wave of similar orientation. Panels (c)-(f) present wave parameters of dominant modes derived from the 2-D CWT: observed wave amplitude $\langle \hat{T} \rangle$, horizontal wavelength λ_{h}, intrinsic propagation direction $\hat{\theta}$, and observed frequency ω. Notably, a peak amplitude exceeding 5 K appears in the southwestern corner of the map, while amplitudes elsewhere remain below 3 K. The distribution of λ_{h} and ω appear patchy which is due overlapping wave structures and we only "cut out" patches where the amplitudes dominate. In the central, north–south-aligned region, horizontal wavelengths as short as $\sim$18 km are found. The peak in $\langle \hat{T} \rangle$ coincides with a region of $\omega \approx 0\,\text{s}^{-1}$. Due to strong westerly winds and an overall observed westward pointing the intrinsic wave propagation direction is entirely westward. Panels (q) and (r) display the distributions of 100 randomly sampled values of the OH*(3-1) layer peak altitude Z_{peak} and thickness Z_{FWHM}. These serve to compute Gaussian-weighted values of Brunt Väisälä frequency N and wind $\boldsymbol{u}$ which themselves are realized as 100 randomly perturbed profiles. Panels (p) and (s) show distributions of the resulting 10,000 OH-weighted N and $\boldsymbol{u}$ values. These represent physically plausible variability stemming from CORAL and SAAMER measurement errors and uncertainties in Z_{peak} and Z_{FWHM} estimation. On that particular instant of time, we find a mean $N = 0.020\,\text{s}^{-1}$ and $\frac{\Delta N}{N} = 25\%$ as well as a mean $|\boldsymbol{u}| = 71.0\,\text{ms}^{-1}$ and $\frac{\Delta|\boldsymbol{u}|}{|\boldsymbol{u}|} = 9.7\%$. Wind direction shows a relative uncertainty of 3.7%. To determine the Δ-quantities, we subtract the 16th from the 84th percentile of the distribution and divide the result by two. Given a normal distribution, this approach would result in one standard deviation. The uncertainty in N is larger than reported in previous studies: Pautet et al. (2021) assumed 10% based on climatology; Vargas (2019) reported 8% from seasonal data from a location about 24° north of our measurement site; and Fritts et al. (2014) achieved 5–6% using sodium lidar measurements. However, these works did

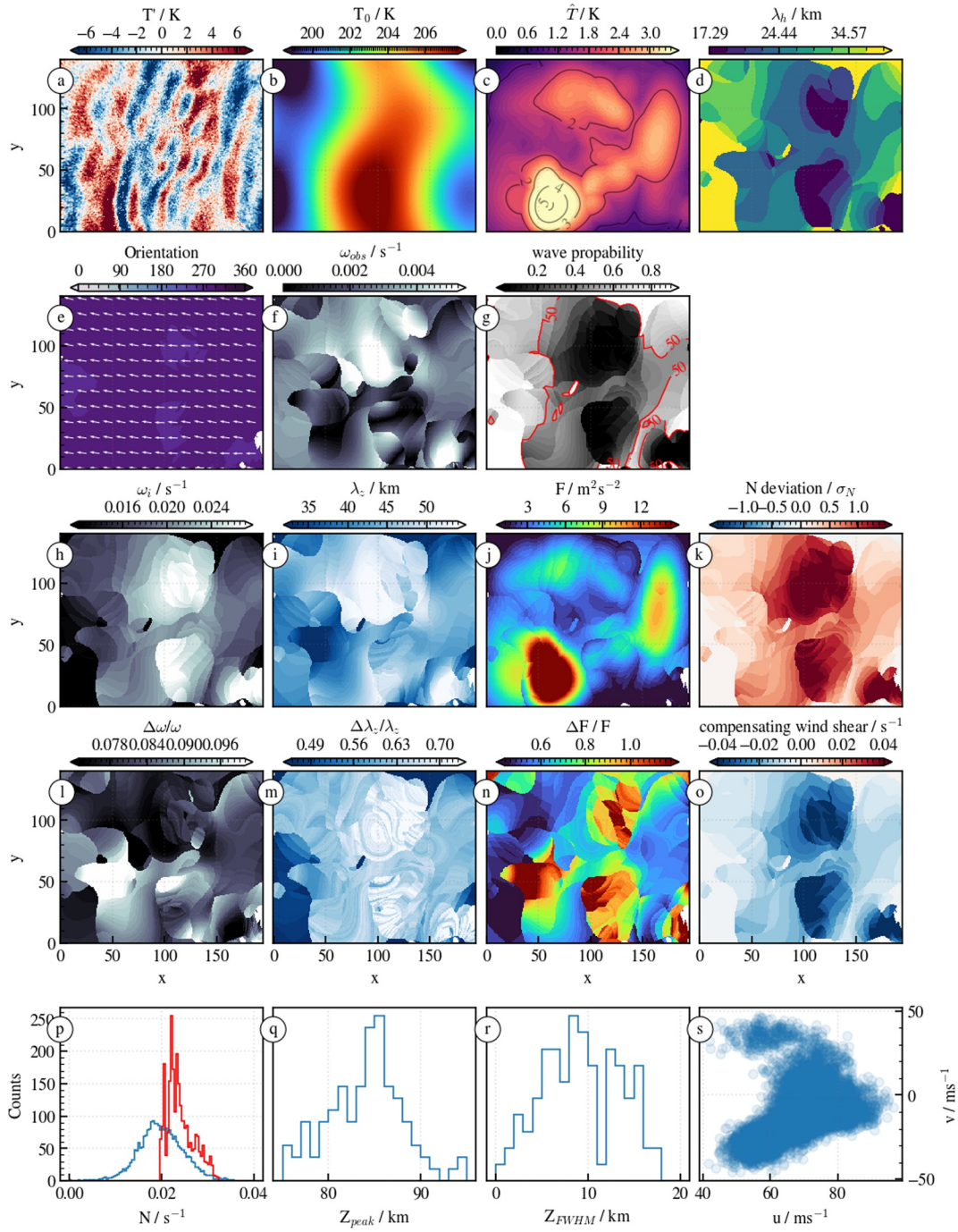

Figure B1. Overview of derived GW properties for the AMTM measurement on the 22 May 2018 at 04:00 UTC. Temperature perturbations (a), background temperature (b) wave amplitude (c), horizontal wavelength (d), propagation direction (e), observed frequency (f), wave probability (g), intrinsic frequency (h), vertical wavelength (i), absolute momentum flux (j), mean N deviation from lidar measurement (k), intrinsic frequency relative uncertainty (l), vertical wavelength relative uncertainty (m), momentum flux relative uncertainty (n), wind shear to enforce propagating wave solution (o), normalized histogram of 10,000 N input values (blue) and N values after wave filtering (red) (p), normalized histogram of 100 randomly chosen Z_{peak} values (q), normalized histogram of 100 randomly chosen Z_{FWHM} values (r), and distribution of 10,000 input (u, v)-pairs (s).

not account for OH*(3-1) layer variability, which—combined with increasing lidar measurement noise—explains the higher uncertainty in our study. Panel (g) shows the wave probability, that is the fraction of propagating wave solutions. Most eye-catching is a north-south oriented region in the central column of the map with values less than 50%. Panels (h)-(n) present the intrinsic frequency $\hat{\omega}$, vertical wavelength λ_z, absolute MF $|\boldsymbol{F}|$, and corresponding relative uncertainties. We notice that the peak MF is co-located with the peak wave amplitude in the southwest. Also, particularly high intrinsic frequencies are found in the middle columnar part of the map. At the location of peak MF, we find $\lambda_h = 22.4\,\mathrm{km}$ (8.7%), $\theta = 283°$ (5.6%), $\langle \hat{T} \rangle = 5.1\,\mathrm{K}$, $\hat{T} = 5.9K$, $\omega \approx 0\,\mathrm{s}^{-1}$, $\hat{\omega} = 0.020\,\mathrm{s}^{-1}$ (9.0%), $\lambda_z = 40\,\mathrm{km}$ (62%), $p_{\mathrm{GW}} = 44.7\%$, $|\boldsymbol{F}| = 30\,\mathrm{m}^2\,\mathrm{s}^{-2}$ (73%). The relative uncertainties provided in brackets are consistent with those in previous studies (Fritts et al., 2014; Pautet et al., 2021; Vargas, 2019). We note that uncertainties in λ_h and θ are only due to the discrete sampling in the 2-D CWT. A dedicated Monte Carlo analysis would be required to propagate AMTM noise (T_{noise}) through the 2-D CWT to assess its effect on derived wave parameters. However, since AMTM data are carefully denoised in preprocessing, we treat wavelet-derived values as effectively exact. Assuming each AMTM pixel represents an independent MF estimate, the FOV-averaged MF uncertainty is 0.3%. While this assumption is optimistic—due to wavelet convolution introducing spatial correlations—we argue that the actual FOV-averaged MF uncertainty lies between 0.3% and 73%. Panel (k) shows the deviation of N in units of σ_N between the average of N as it finds entry into our MC^2-MF retrieval and the median of N after applying our wave filter criteria from Section 3.2. The short scales and the high intrinsic frequency in the central column of the map indicates wave reflection and therefore a region where waves become evanescent. Only the fraction of the distributions where N is large, wave solutions are still real-valued, hence propagating. There are three possible interpretations: (a) The waves are truly evanescent, which seems unlikely given the simultaneous detection of MWs in sodium and oxygen airglow layers (see Figures S3 and S4 in Supporting Information S1). (b) N is systematically underestimated, which would require a consistent underestimation of vertical temperature gradients. (c) A large-scale GW modulates the vertical shear field, enabling otherwise evanescent modes to propagate. We have converted the deviation in N into a vertical shear field (panel o) and find values exceeding $-20\mathrm{ms}^{-1}\mathrm{km}^{-1}$ in the central domain, supporting the third interpretation and suggesting wave-wave interactions between small- and large-scale GWs.

Conflict of Interest

The authors declare no conflicts of interest relevant to this study.

Availability Statement

JAWARA data (Sato & Koshin, 2025) is publicly available as netCDF files. The AMTM, CORAL, and SAAMER data are available at Zenodo (Reichert, Pautet, et al., 2025). Analysis scripts for this study are available via Zenodo (Reichert, Ungermann, & Rhode, 2025). The full data set and accompanying code are made publicly available under a CC-BY license.

Acknowledgments

RR gratefully acknowledges funding from the German Research Foundation (DFG; Grant RE 5127/1-1). The AMTM operated at Río Grande was designed and built at Utah State University (USU) and the Space Dynamics Laboratory (SDL) with support from the NSF Grant 1061892. It was operated under NSF Grant 1651233. We extend our sincere thanks to the team at the Estación Astronómica Río Grande for their technical support and warm hospitality. KS is supported by JSPS KAKENHI Grant JP22H00169. RR thanks colleagues from the German Aerospace Center such as Michael Binder, Andreas Dörnbrack, Christopher Geach, Sonja Gisinger, Natalie Kaifler, and Markus Rapp for helpful discussions and valuable comments. RR is grateful to Corwin Wright and Neil Hindley for valuable discussions on scientific writing and spectral analysis. We especially thank Neil Hindley for providing the processed SAAMER wind data. Our appreciation goes to Andreas Dörnbrack for providing the IFS data. RR acknowledges the use of the color blindness simulator (COBLIS). Finally, RR acknowledges the use of ChatGPT (OpenAI) to refine the structure and scientific tone of the manuscript. Open Access funding enabled and organized by Projekt DEAL.

References

Alexander, M. J., & Teitelbaum, H. (2011). Three-dimensional properties of Andes Mountain waves observed by satellite: A case study. *Journal of Geophysical Research*, *116*(D23), D23110. https://doi.org/10.1029/2011JD016151

Baker, D. J., & Stair, A., Jr. (1988). Rocket measurements of the altitude distributions of the hydroxyl airglow. *Physica Scripta*, *37*(4), 611–622. https://doi.org/10.1088/0031-8949/37/4/021

Becker, E., & Vadas, S. L. (2020). Explicit global simulation of gravity waves in the thermosphere. *Journal of Geophysical Research: Space Physics*, *125*(10), e2020JA028034. https://doi.org/10.1029/2020JA028034

Bossert, K., Fritts, D. C., Pautet, P.-D., Williams, B. P., Taylor, M. J., Kaifler, B., et al. (2015). Momentum flux estimates accompanying multiscale gravity waves over Mount Cook, New Zealand, on 13 July 2014 during the DEEPWAVE campaign. *Journal of Geophysical Research: Atmospheres*, *120*(18), 9323–9337. https://doi.org/10.1002/2015JD023197

Bossert, K., Kruse, C. G., Heale, C. J., Fritts, D. C., Williams, B. P., Snively, J. B., et al. (2017). Secondary gravity wave generation over New Zealand during the DEEPWAVE campaign. *Journal of Geophysical Research: Atmospheres*, *122*(15), 7834–7850. https://doi.org/10.1002/2016JD026079

Bramberger, M., Dörnbrack, A., Bossert, K., Ehard, B., Fritts, D. C., Kaifler, B., et al. (2017). Does strong tropospheric forcing cause large-amplitude mesospheric gravity waves? A DEEPWAVE case study. *Journal of Geophysical Research: Atmospheres*, *122*(21), 11–422. https://doi.org/10.1002/2017JD027371

de la Torre, A., Alexander, P., Hierro, R., Llamedo, P., Rolla, A., Schmidt, T., & Wickert, J. (2012). Large-amplitude gravity waves above the southern Andes, the Drake Passage, and the Antarctic Peninsula. *Journal of Geophysical Research*, *117*(D2), D02106. https://doi.org/10.1029/2011JD016377

Dewan, E., & Picard, R. (2001). On the origin of mesospheric bores. *Journal of Geophysical Research*, *106*(D3), 2921–2927. https://doi.org/10.1029/2000JD900697

Dörnbrack, A., Birner, T., Fix, A., Flentje, H., Meister, A., Schmid, H., et al. (2002). Evidence for inertia gravity waves forming polar stratospheric clouds over Scandinavia. *Atmosphere*, *107*(D20), SOL30-1–SOL30-18. https://doi.org/10.1029/2001JD000452

Dunker, T. (2018). The airglow layer emission altitude cannot be determined unambiguously from temperature comparison with lidar. *Atmospheric Chemistry and Physics*, *18*(9), 6691–6697. https://doi.org/10.5194/acp-18-6691-2018

Eckermann, S. D. (1992). Ray-tracing simulation of the global propagation of inertia gravity waves through the zonally averaged middle atmosphere. *Journal of Geophysical Research*, *97*(D14), 15849–15866. https://doi.org/10.1029/92JD01410

Ehard, B., Kaifler, B., Dörnbrack, A., Preusse, P., Eckermann, S. D., Bramberger, M., et al. (2017). Horizontal propagation of large-amplitude mountain waves into the polar night jet. *Journal of Geophysical Research: Atmospheres*, *122*(3), 1423–1436. https://doi.org/10.1002/2016JD025621

Fritts, D. C. (1982). Shear excitation of atmospheric gravity waves. *Journal of the Atmospheric Sciences*, *39*(9), 1936–1952. https://doi.org/10.1175/1520-0469(1982)039⟨1936:SEOAGW⟩2.0.CO;2

Fritts, D. C., & Alexander, M. J. (2003). Gravity wave dynamics and effects in the middle atmosphere. *Reviews of Geophysics*, *41*(1), 1003. https://doi.org/10.1029/2001RG000106

Fritts, D. C., Janches, D., Iimura, H., Hocking, W., Mitchell, N. J., Stockwell, R., et al. (2010). Southern Argentina agile meteor radar: System design and initial measurements of large-scale winds and tides. *Journal of Geophysical Research*, *115*(D18), D18112. https://doi.org/10.1029/2010JD013850

Fritts, D. C., Lund, T. S., Wan, K., & Liu, H.-L. (2021). Numerical simulation of mountain waves over the southern Andes. Part II: Momentum fluxes and wave–mean-flow interactions. *Journal of the Atmospheric Sciences*, *78*(10), 3069–3088. https://doi.org/10.1175/JAS-D-20-0207.1

Fritts, D. C., Pautet, P.-D., Bossert, K., Taylor, M. J., Williams, B. P., Iimura, H., et al. (2014). Quantifying gravity wave momentum fluxes with mesosphere temperature mappers and correlative instrumentation. *Journal of Geophysical Research: Atmospheres*, *119*(24), 13–583. https://doi.org/10.1002/2014JD022150

Greenhow, J., & Neufeld, E. (1959). Measurements of turbulence in the 80-to 100-km region from the radio echo observations of meteors. *Journal of Geophysical Research*, *64*(12), 2129–2133. https://doi.org/10.1029/JZ064i012p02129

Harvey, V. L., Pedatella, N., Becker, E., & Randall, C. (2022). Evaluation of polar winter mesopause wind in WACCMX+ DART. *Journal of Geophysical Research: Atmospheres*, *127*(15), e2022JD037063. https://doi.org/10.1029/2022JD037063

Hauchecorne, A., & Chanin, M.-L. (1980). Density and temperature profiles obtained by lidar between 35 and 70 km. *Geophysical Research Letters*, *7*(8), 565–568. https://doi.org/10.1029/GL007i008p00565

Hecht, J., Fritts, D., Wang, L., Gelinas, L., Rudy, R., Walterscheid, R. L., et al. (2018). Observations of the breakdown of mountain waves over the Andes lidar observatory at Cerro Pachon on 8/9 July 2012. *Journal of Geophysical Research: Atmospheres*, *123*(1), 276–299. https://doi.org/10.1002/2017JD027303

Hecht, J., Walterscheid, R., & Vincent, R. (2001). Airglow observations of dynamical (wind shear-induced) instabilities over Adelaide, Australia, associated with atmospheric gravity waves. *Journal of Geophysical Research*, *106*(D22), 28189–28197. https://doi.org/10.1029/2001JD000419

Hersbach, H., Bell, B., Berrisford, P., Hirahara, S., Horányi, A., Muñoz-Sabater, J., et al. (2020). The ERA5 global reanalysis. *Quarterly Journal of the Royal Meteorological Society*, *146*(730), 1999–2049. https://doi.org/10.1002/qj.3803

Hindley, N. P., Mitchell, N. J., Cobbett, N., Smith, A. K., Fritts, D. C., Janches, D., et al. (2022). Radar observations of winds, waves and tides in the mesosphere and lower thermosphere over south Georgia island (54 S, 36 W) and comparison with WACCM simulations. *Atmospheric Chemistry and Physics*, *22*(14), 9435–9459. https://doi.org/10.5194/acp-22-9435-2022

Hindley, N. P., Smith, N. D., Wright, C. J., Rees, D. A. S., & Mitchell, N. J. (2016). A two-dimensional stockwell transform for gravity wave analysis of AIRS measurements. *Atmospheric Measurement Techniques*, *9*(6), 2545–2565. https://doi.org/10.5194/amt-9-2545-2016

Hines, C. O. (1960). Internal atmospheric gravity waves at ionospheric heights. *Canadian Journal of Physics*, *38*(11), 1441–1481. https://doi.org/10.1139/p60-150

Kaifler, B., & Kaifler, N. (2021). A Compact Rayleigh Autonomous Lidar (CORAL) for the middle atmosphere. *Atmospheric Measurement Techniques*, *14*(2), 1715–1732. https://doi.org/10.5194/amt-14-1715-2021

Kaifler, B., Kaifler, N., Ehard, B., Dörnbrack, A., Rapp, M., & Fritts, D. C. (2015). Influences of source conditions on mountain wave penetration into the stratosphere and mesosphere. *Geophysical Research Letters*, *42*(21), 9488–9494. https://doi.org/10.1002/2015GL066465

Kaifler, N., Kaifler, B., Dörnbrack, A., Rapp, M., Hormaechea, J. L., & de la Torre, A. (2020). Lidar observations of large-amplitude mountain waves in the stratosphere above Tierra del Fuego, Argentina. *Scientific Reports*, *10*(1), 14529. https://doi.org/10.1038/s41598-020-71443-7

Kjellstrand, C. B., Fritts, D. C., Miller, A. D., Williams, B. P., Kaifler, N., Geach, C., et al. (2022). Multi-scale kelvin-Helmholtz instability dynamics observed by PMC turbo on 12 July 2018: 1. Secondary instabilities and billow interactions. *Journal of Geophysical Research: Atmospheres*, *127*(18), e2021JD036232. https://doi.org/10.1029/2021jd036232

Kogure, M., Yue, J., Nakamura, T., Hoffmann, L., Vadas, S. L., Tomikawa, Y., et al. (2020). First direct observational evidence for secondary gravity waves generated by mountain waves over the Andes. *Geophysical Research Letters*, *47*(17), e2020GL088845. https://doi.org/10.1029/2020GL088845

Koshin, D., Kohma, M., & Sato, K. (2022a). Characteristics of the intraseasonal oscillation in the equatorial mesosphere and lower thermosphere region revealed by satellite observation and global analysis by the jaguar data assimilation system. *Journal of Geophysical Research: Atmospheres*, *127*(16), e2022JD036816. https://doi.org/10.1029/2022JD036816

Koshin, D., Sato, K., Kohma, M., & Watanabe, S. (2022b). An update on the 4D-LETKF data assimilation system for the whole neutral atmosphere. *Geoscientific Model Development*, *15*(5), 2293–2307. https://doi.org/10.5194/gmd-15-2293-2022

Koshin, D., Sato, K., Watanabe, S., & Miyazaki, K. (2025). The JAGUAR-DAS whole neutral atmosphere reanalysis: JAWARA. *Progress in Earth and Planetary Science*, *12*(1), 1. https://doi.org/10.1186/s40645-024-00674-3

Krasauskas, L., Kaifler, B., Rhode, S., Ungermann, J., Woiwode, W., & Preusse, P. (2023). Oblique propagation and refraction of gravity waves over the Andes observed by GLORIA and ALIMA during the southTRAC campaign. *Journal of Geophysical Research: Atmospheres*, *128*(10), e2022JD037798. https://doi.org/10.1029/2022JD037798

Krassovsky, V., Kuzmin, K., Piterskaya, N., Semenov, A., Shagaev, M., Shefov, N., & Toroshelidze, T. (1975). Results of some airglow observations of internal gravitational waves. *Planetary and Space Science*, *23*(5), 896–898. https://doi.org/10.1016/0032-0633(75)90027-6

Kruse, C. G., Smith, R. B., & Eckermann, S. D. (2016). The midlatitude lower-stratospheric mountain wave "valve layer". *Journal of the Atmospheric Sciences*, *73*(12), 5081–5100. https://doi.org/10.1175/JAS-D-16-0173.1

Liu, X., Xu, J., Yue, J., Vadas, S. L., & Becker, E. (2019). Orographic primary and secondary gravity waves in the middle atmosphere from 16-year SABER observations. *Geophysical Research Letters*, *46*(8), 4512–4522. https://doi.org/10.1029/2019GL082256

Lund, T. S., Fritts, D. C., Wan, K., Laughman, B., & Liu, H.-L. (2020). Numerical simulation of mountain waves over the southern Andes. Part I: Mountain wave and secondary wave character, evolutions, and breaking. *Journal of the Atmospheric Sciences*, *77*(12), 4337–4356. https://doi.org/10.1175/JAS-D-19-0356.1

Manning, L., Villard, O., & Peterson, A. (1950). Meteoric echo study of upper atmosphere winds. *Proceedings of the IRE*, *38*(8), 877–883. https://doi.org/10.1109/JRPROC.1950.234124

Maraun, D., & Kurths, J. (2004). Cross wavelet analysis: Significance testing and pitfalls. *Nonlinear Processes in Geophysics*, *11*(4), 505–514. https://doi.org/10.5194/npg-11-505-2004

Marks, C. J., & Eckermann, S. D. (1995). A three-dimensional nonhydrostatic ray-tracing model for gravity waves: Formulation and preliminary results for the middle atmosphere. *Journal of the Atmospheric Sciences*, *52*(11), 1959–1984. https://doi.org/10.1175/1520-0469(1995)052⟨1959:ATDNRT⟩2.0.CO;2

Mixa, T., Dörnbrack, A., & Rapp, M. (2021). Nonlinear simulations of gravity wave tunneling and breaking over Auckland Island. *Journal of the Atmospheric Sciences*, *78*(5), 1567–1582. https://doi.org/10.1175/JAS-D-20-0230.1

Moreels, G., & Herse, M. (1977). Photographic evidence of waves around the 85 km level. *Planetary and Space Science*, *25*(3), 265–273. https://doi.org/10.1016/0032-0633(77)90137-4

Nappo, C. J. (2013). *An introduction to atmospheric gravity waves*. Academic Press.

Noxon, J. (1978). Effect of internal gravity waves upon night airglow temperatures. *Geophysical Research Letters*, *5*(1), 25–27. https://doi.org/10.1029/GL005i001p00025

Pautet, P.-D., Taylor, M., Fritts, D. C., Janches, D., Kaifler, N., Dörnbrack, A., & Hormaechea, J. L. (2021). Mesospheric mountain wave activity in the lee of the southern Andes. *Journal of Geophysical Research: Atmospheres*, *126*(7), e2020JD033268. https://doi.org/10.1029/2020JD033268

Pautet, P.-D., Taylor, M. J., Fritts, D., Bossert, K., Williams, B., Broutman, D., et al. (2016). Large-amplitude mesospheric response to an orographic wave generated over the southern ocean Auckland islands (50.7 S) during the deepwave project. *Journal of Geophysical Research: Atmospheres*, *121*(4), 1431–1441. https://doi.org/10.1002/2015JD024336

Pautet, P.-D., Taylor, M. J., Pendleton, W., Zhao, Y., Yuan, T., Esplin, R., & McLain, D. (2014). Advanced mesospheric temperature mapper for high-latitude airglow studies. *Applied Optics*, *53*(26), 5934–5943. https://doi.org/10.1364/AO.53.005934

Peterson, A., & Kieffaber, L. (1973). Infrared photography of OH airglow structures. *Nature*, *242*(5396), 321–322. https://doi.org/10.1038/242321a0

Rapp, M., Kaifler, B., Dörnbrack, A., Gisinger, S., Mixa, T., Reichert, R., et al. (2021). SOUTHTRAC-GW: An airborne field campaign to explore gravity wave dynamics at the world's strongest hotspot. *Bulletin America Meteorology Social*, *102*(4), E871–E893. https://doi.org/10.1175/BAMS-D-20-0034.1

Reichert, R., Kaifler, B., Kaifler, N., Dörnbrack, A., Rapp, M., & Hormaechea, J. L. (2021). High-cadence lidar observations of middle atmospheric temperature and gravity waves at the southern Andes hot spot. *Journal of Geophysical Research: Atmospheres*, *126*(22), e2021JD034683. https://doi.org/10.1029/2021JD034683

Reichert, R., Kaifler, B., Kaifler, N., Rapp, M., Pautet, P.-D., Taylor, M. J., et al. (2019). Retrieval of intrinsic mesospheric gravity wave parameters using lidar and airglow temperature and meteor radar wind data. *Atmospheric Measurement Techniques*, *12*(11), 5997–6015. https://doi.org/10.5194/amt-12-5997-2019

Reichert, R., Pautet, D., Kaifler, B., Janches, D., & Smith, S. (2025). AMTM, CORAL, and SAAMER atmospheric observations as well as analysis products. *Zenodo*. https://doi.org/10.5281/zenodo.16414582

Reichert, R., Ungermann, J., & Rhode, S. (2025). *Analysis scripts for atmospheric wave diagnostics*. Zenodo. https://doi.org/10.5281/zenodo.16950913

Sato, K., & Koshin, D. (2025). JAGUAR data assimilation system whole neutral atmosphere reanalysis (JAWARA) [Dataset]. https://doi.org/10.17592/002.2025010407

Sato, K., Tateno, S., Watanabe, S., & Kawatani, Y. (2012). Gravity wave characteristics in the southern hemisphere revealed by a high-resolution middle-atmosphere general circulation model. *Journal of the Atmospheric Sciences*, *69*(4), 1378–1396. https://doi.org/10.1175/JAS-D-11-0101.1

Sato, K., Tomikawa, Y., Kohma, M., Yasui, R., Koshin, D., Okui, H., et al. (2023). Interhemispheric coupling study by observations and modelling (ICSOM): Concept, campaigns, and initial results. *Journal of Geophysical Research: Atmospheres*, *128*(11), e2022JD038249. https://doi.org/10.1029/2022JD038249

Scorer, R. (1951). Gravity waves in the atmosphere. Archiv für Meteorologie, Geophysik und Bioklimatologie. *Serie*, *A*(4), 176–193. https://doi.org/10.1007/BF02246801

Sedlak, R., Hannawald, P., Schmidt, C., Wüst, S., & Bittner, M. (2016). High-resolution observations of small-scale gravity waves and turbulence features in the OH airglow layer. *Atmospheric Measurement Techniques*, *9*(12), 5955–5963. https://doi.org/10.5194/amt-9-5955-2016

Smith, S. M., Taylor, M. J., Swenson, G. R., She, C.-Y., Hocking, W., Baumgardner, J., & Mendillo, M. (2003). A multidiagnostic investigation of the mesospheric bore phenomenon. *Journal of Geophysical Research*, *108*(A2). https://doi.org/10.1029/2002JA009500

Stober, G., Janches, D., Matthias, V., Fritts, D., Marino, J., Moffat-Griffin, T., et al. (2021). Seasonal evolution of winds, atmospheric tides, and Reynolds stress components in the southern hemisphere mesosphere–lower thermosphere in 2019. *Annales Geophysicae*, *39*, 1–29. https://doi.org/10.5194/angeo-39-1-2021

Taylor, M. J., Pautet, P.-D., Medeiros, A. F., Buriti, R., Fechine, J., Fritts, D. C., et al. (2009). Characteristics of mesospheric gravity waves near the magnetic equator, Brazil, during the SpreadFEx campaign. *Annales Geophysicae*, *27*(2), 461–472. https://doi.org/10.5194/angeo-27-461-2009

Taylor, M. J., Ryan, E., Tuan, T., & Edwards, R. (1993). Evidence of preferential directions for gravity wave propagation due to wind filtering in the middle atmosphere. *Journal of Geophysical Research*, *98*(A4), 6047–6057. https://doi.org/10.1029/92JA02604

Torrence, C., & Compo, G. P. (1998). A practical guide to wavelet analysis. *Bulletin America Meteorology Social*, *79*(1), 61–78. https://doi.org/10.1175/1520-0477(1998)079⟨0061:APGTWA⟩2.0.CO;2

Ungermann, J., & Reichert, R. (2025). JuWavelet—Continuous wavelet transform and *S* transform for wave analysis. *Geoscientific Model Development*, *18*(22), 8613–8626. https://doi.org/10.5194/gmd-18-8613-2025

Vadas, S. L., & Azeem, I. (2021). Concentric secondary gravity waves in the thermosphere and ionosphere over the continental United States on March 25–26, 2015 from deep convection. *Journal of Geophysical Research: Space Physics*, *126*(2), e2020JA028275. https://doi.org/10.1029/2020JA028275

Vadas, S. L., & Becker, E. (2019). Numerical modeling of the generation of tertiary gravity waves in the mesosphere and thermosphere during strong mountain wave events over the southern Andes. *Journal of Geophysical Research: Space Physics*, *124*(9), 7687–7718. https://doi.org/10.1029/2019JA026694

Vadas, S. L., Becker, E., Bossert, K., Baumgarten, G., Hoffmann, L., & Harvey, V. L. (2023). Secondary gravity waves from the stratospheric polar vortex over ALOMAR observatory on 12–14 January 2016: Observations and modeling. *Journal of Geophysical Research: Atmospheres*, *128*(2), e2022JD036985. https://doi.org/10.1029/2022JD036985

Vadas, S. L., Zhao, J., Chu, X., & Becker, E. (2018). The excitation of secondary gravity waves from local body forces: Theory and observation. *Journal of Geophysical Research: Atmospheres*, *123*(17), 9296–9325. https://doi.org/10.1029/2017JD027970

Vargas, F. (2019). Uncertainties in gravity wave parameters, momentum fluxes, and flux divergences estimated from multi-layer measurements of mesospheric nightglow layers. *Advances in Space Research*, *63*(2), 967–985. https://doi.org/10.1016/j.asr.2018.09.039

Wedi, N., Bauer, P., Denoninck, W., Diamantakis, M., Hamrud, M., Kuhnlein, C., et al. (2015). The modelling infrastructure of the integrated forecasting system: Recent advances and future challenges.

Wright, C. J., Hindley, N. P., Alexander, M. J., Holt, L. A., & Hoffmann, L. (2021). Using vertical phase differences to better resolve 3d gravity wave structure. *Atmospheric Measurement Techniques*, *14*(9), 5873–5886. https://doi.org/10.5194/amt-14-5873-2021

Wright, C. J., Hindley, N. P., Hoffmann, L., Alexander, M. J., & Mitchell, N. J. (2017). Exploring gravity wave characteristics in 3-D using a novel S-transform technique: AIRS/Aqua measurements over the southern Andes and Drake Passage. *Atmospheric Chemistry and Physics*, *17*(13), 8553–8575. https://doi.org/10.5194/acp-17-8553-2017

Yasui, R., Sato, K., & Miyoshi, Y. (2018). The momentum budget in the stratosphere, mesosphere, and lower thermosphere. Part II: The in situ generation of gravity waves. *Journal of the Atmospheric Sciences*, *75*(10), 3635–3651. https://doi.org/10.1175/JAS-D-17-0337.1

Yue, J., She, C.-Y., Nakamura, T., Harrell, S., & Yuan, T. (2010). Mesospheric bore formation from large-scale gravity wave perturbations observed by collocated all-sky OH imager and sodium lidar. *Journal of Atmospheric and Solar-Terrestrial Physics*, *72*(1), 7–18. https://doi.org/10.1016/j.jastp.2009.10.002

Zhao, Y., Taylor, M. J., & Chu, X. (2005). Comparison of simultaneous Na lidar and mesospheric nightglow temperature measurements and the effects of tides on the emission layer heights. *Journal of Geophysical Research*, *110*(D9), D09S07. https://doi.org/10.1029/2004JD005115